No Title Page

Department of Geophysics and Astronomy

The University of British Columbia
2075 Wesbrook Place
Vancouver, Canada
V6T 1W5

Date August 22, 1978.

ABSTRACT

An 80 km seismic refraction line was recorded on an array of three ocean bottom seismometers located 5 km west of the northern tip of Explorer ridge and parallel to Revere-Dellwood fracture zone on the Pacific plate. One reversed and two split-spread profiles have been obtained. The combined use of rotated SV component and polarization filtered record sections enabled identification and timing of the refracted S-wave on most sections. The travel time - distance relation for both P and S waves is interpreted in the intercept time (tau) and ray parameter domain using the technique introduced by Bessonova et al. (1974). This enables application of tau inversion to give extremal bounds for velocity-depth curves. A linearized inversion technique is applied to give the smoothest velocity-depth profiles consistent with the travel time data. Amplitude analysis using disk ray theory synthetic seismograms further refine the P-wave velocity-depth models.

The final P- and S-wave velocity-depth profiles show a general increase of velocity with depth and no distinct structural discontinuities. A normal oceanic crustal thickness of approximately 6.5 km and an anomalously low Pn velocity of 7.3 km sec^{-1} are interpreted. The existence of an abnormally thick crust (8-10 km) on the opposite side of the ridge in Explorer plate, determined in other studies, contrasts markedly with the results of this research. Such a contrast lends support to the proposal that the complex

structure and thick crust are the result of compressive interaction between the young, small Explorer plate and the older, larger North America plate. Values of Poisson's ratio in the range of 0.25 to 0.32 are determined for the crustal material but better resolution of the velocity-depth profiles is required before a meaningful geological interpretation can be made.

TABLE OF CONTENTS

LIST OF TABLES

LIST OF FIGURES

ACKNOWLEDGEMENTS

I wish to take this opportunity to express my deepest appreciation to Dr. R.M.Clowes; without his initiation, encouragement, guidance and long hours of discussion, this project could not have been completed so smoothly.

Fruitful ideas from Dr. R.D.Hyndman were invaluable. Helpful discussions with Dr. D.W.Oldenburg and Dr. T.J.Ulyrch are gratefully acknowledged. Discussions with Mr. G.A.McMechan and Mr. A.J.Thorleifson were useful and stimulating. I also wish to thank Dr. E.E.Davis, Dr. T.Lewis, Dr. C.R.B.Lister, Mr. D.L.Barrett, Mr. M.N.Bone, Mr. S.Lynch, Mr. G.C.Rogers, Mr. D.Seemann, Mr. U.S.Wade and again to Dr. R.D.Hyndman for their invaluable contribution in collecting the data. Further, I wish to express my gratitude to the officers and crew on board C.F.A.V. ENDEAVOUR for their assistance during the cruise. Explosive experts provided by the Fleet Diving Unit, Pacific Maritime Command, Esquimalt B.C. are gratefully acknowledged. Dr. R.A.Wiggins provided a copy of his computer routines HRGLTZ and MDLPLT.

Financial support for this project was provided by a research contract and research agreement from the Earth Physics Branch, Department of Energy, Mines and Resources and by the National Research Council of Canada operating grant A7707. Additional funding was obtained from Mobil Oil Canada Ltd., Shell Canada Resources Ltd., and Chevron Standard Ltd.

1. INTRODUCTION

Because of its interesting and complex tectonic environment, the region off Canada's west coast has continuously attracted the attention of many earth scientists (Vine and Matthews,1963; Vine and Wilson,1965; Vine,1966; McKenzie and Parker,1967; Tobin and Sykes,1968; Atwater,1970; Silver,1971; Crosson,1972; Srivastava,1973; Stacey,1973; Barr and Chase,1974; Chase et al.,1975; Riddihough and Hyndman,1976; Dickinson,1976; Riddihough,1977). An inferred trench, spreading centres and transform faults are all present; these outline the boundaries of the four active plates (see Figures 1.1 and 1.2). The two smaller plates, Explorer and Juan de Fuca, wedged between the two larger plates, Pacific and North America, have reoriented themselves in the last 10 m.y. (Riddihough,1977). Of particular importance in this study is the adjustment of the en-echelon spreading ridges, and probably also the small plates, to the approaching trench. Previous deep seismic sounding surveys in the region have revealed complex crustal structure in Winona basin to the northeast of Explorer ridge (Lynch,1977; Thorleifson,1978) and on Explorer plate east of the ridge (Malecek and Clowes,1978). The complex structures are inferred to be the result of interaction with the North America plate. The question of whether or not the western flank of Explorer ridge has a normal crustal structure led to the 1976 deep seismic sounding survey using ocean-bottom

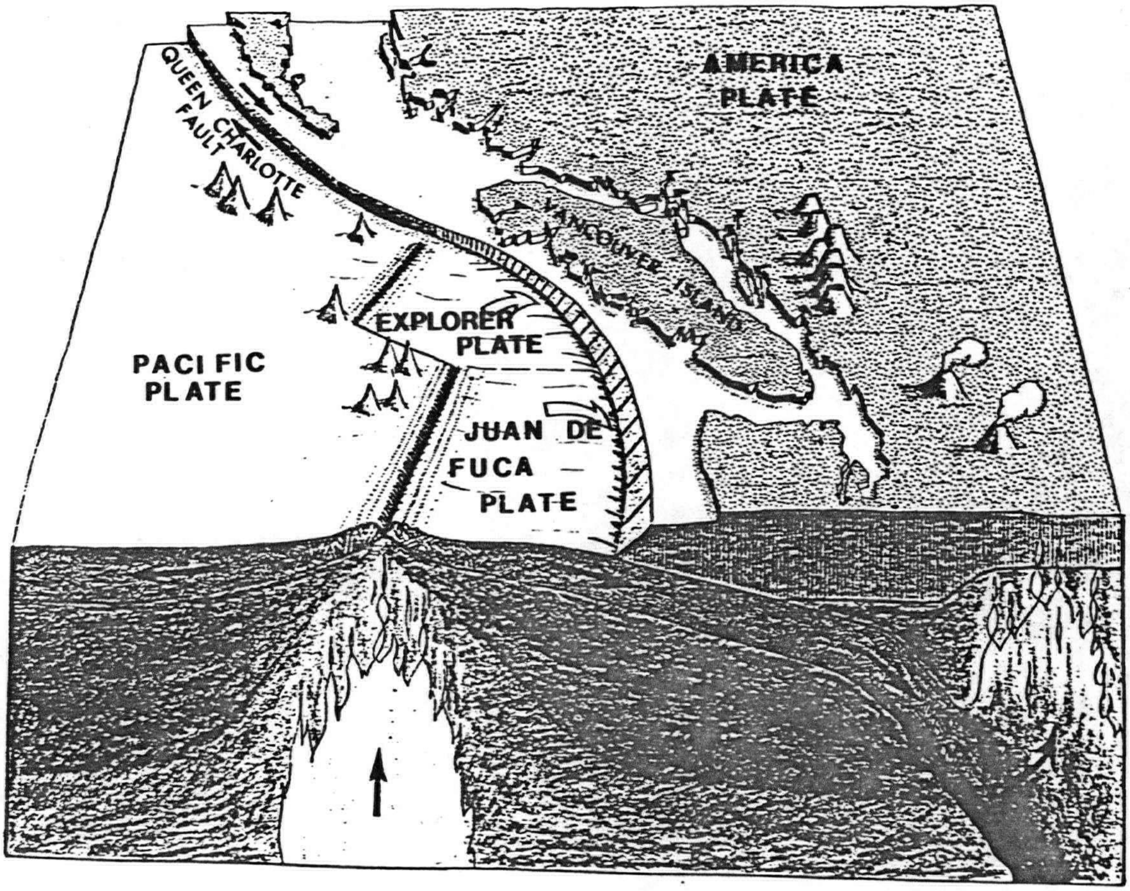

Figure 1.1 Artistic conception of a general tectonic picture for Canada's west coast (after Riddihough and Carnes, unpublished work).

seismometers (OBS's).

1.1 Tectonic setting of the study area :

According to Atwater (1970), the tectonic setting of the North Pacific 80 m.y. ago included a large ridge/transform fault system similar to that in the present South Atlantic. Two ancient oceanic plates, the Kula and Farallon, and part of the Pacific plate, all of which were associated with the ridge system, have been overridden by the North American plate. Unstable triple point junctions (McKenzie and Morgan, 1969) have led to both the activation and annihilation of trenches and transform faults with the accompanying reorientation of plate motions and spreading directions. The Juan de Fuca plate is now believed to be a remnant of the subducted Farallon plate.

Recent detailed re-examination of the magnetic anomaly patterns in the north-eastern Pacific by Riddihough (1977) has demonstrated that the northern end of Juan de Fuca plate has been moving independently with respect to its southern associate for the last 7 m.y. Consequently, the name Explorer plate is designated to distinguish it from the original Juan de Fuca plate. In fact, the presence of the Nootka fault zone as the boundary of the two plates was confirmed during a recent geophysical cruise (R.D. Hyndman, personal communication, 1977).

The major tectonic features off Canada's west coast are summarized in Figure 1.2. Based on various geophysical findings, Riddihough and Hyndman (1976) have convincingly argued that subduction is presently taking place along the west coast of British Columbia south of 50°N. The Queen Charlotte transform fault between the Pacific and the North America plates is presently active and well defined north of 51°N. The plate boundary between 50°N and 51°N probably is associated with oblique subduction (Riddihough,1977; Thorleifson,1978). To the west, the boundary of Explorer plate is well defined by a series of fracture zones and spreading centres (see Figure 1.2). The transform fault extending northwest from Dellwood knolls and the associated Tuzo Wilson seamounts (formerly J. Tuzo Wilson knolls) are seismically active. As well, the fresh volcanic rock dredged from Tuzo Wilson seamounts also indicates that this feature is an active spreading centre (Chase,1977).

Explorer ridge and Revere-Dellwood fracture zone form the major part of the western boundary of Explorer plate. Bathymetrically, Explorer ridge is poorly outlined; the locus of the spreading centre was originally defined by its magnetic signature. Figure 1.3 shows the interpreted ridges as the stippled region overlain on a bathymetric map. The southern end of the ridge is clearly traceable, whereas the northern end bifurcates into two poorly defined segments which have a trough-like character. Based on a recent seismicity study, Hyndman et al. (1978) conclude that both segments of the ridge are presently active although the northwest segment is believed to be responsible for most of the spreading.

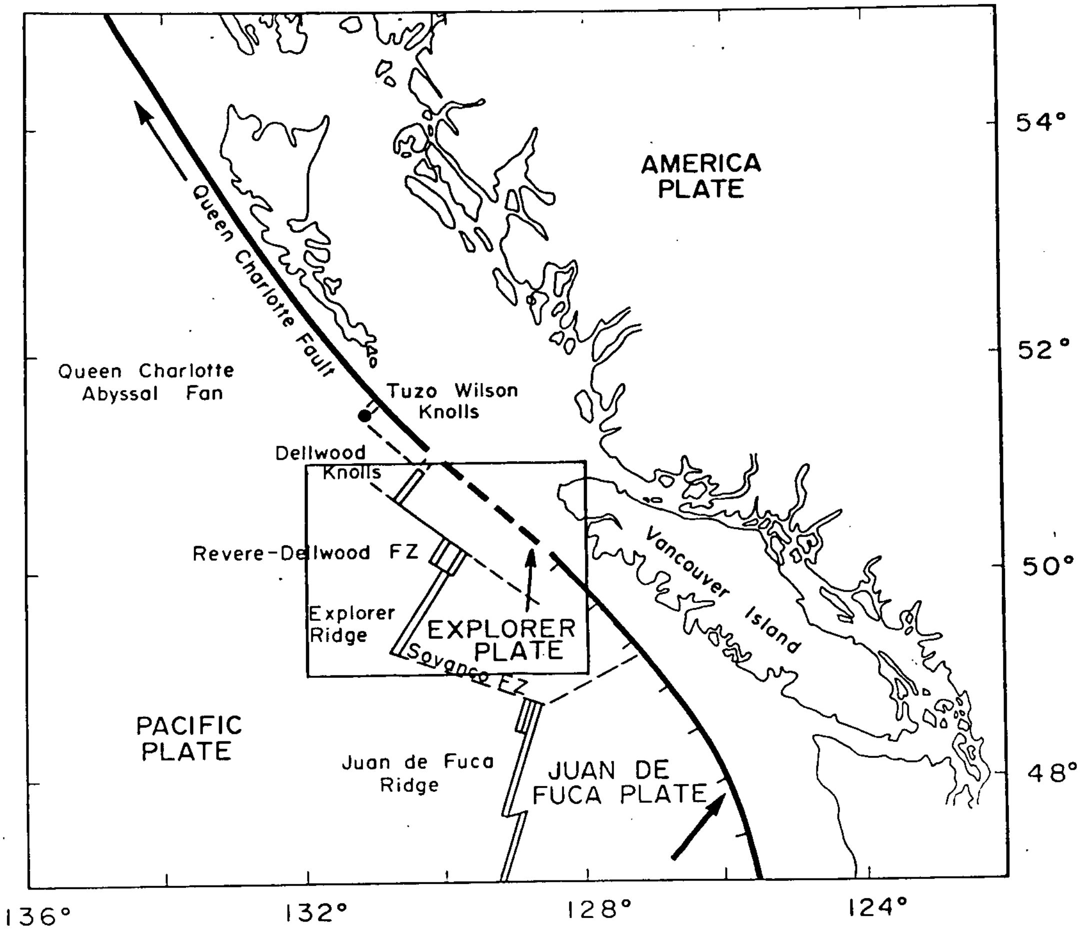

Figure 1.2 Major plate boundaries off Canada's west coast. Arrows show directions of plate motions relative to the America plate (after Riddihough,1977). The square block outlines the study area shown in detail in Figure 1.3.

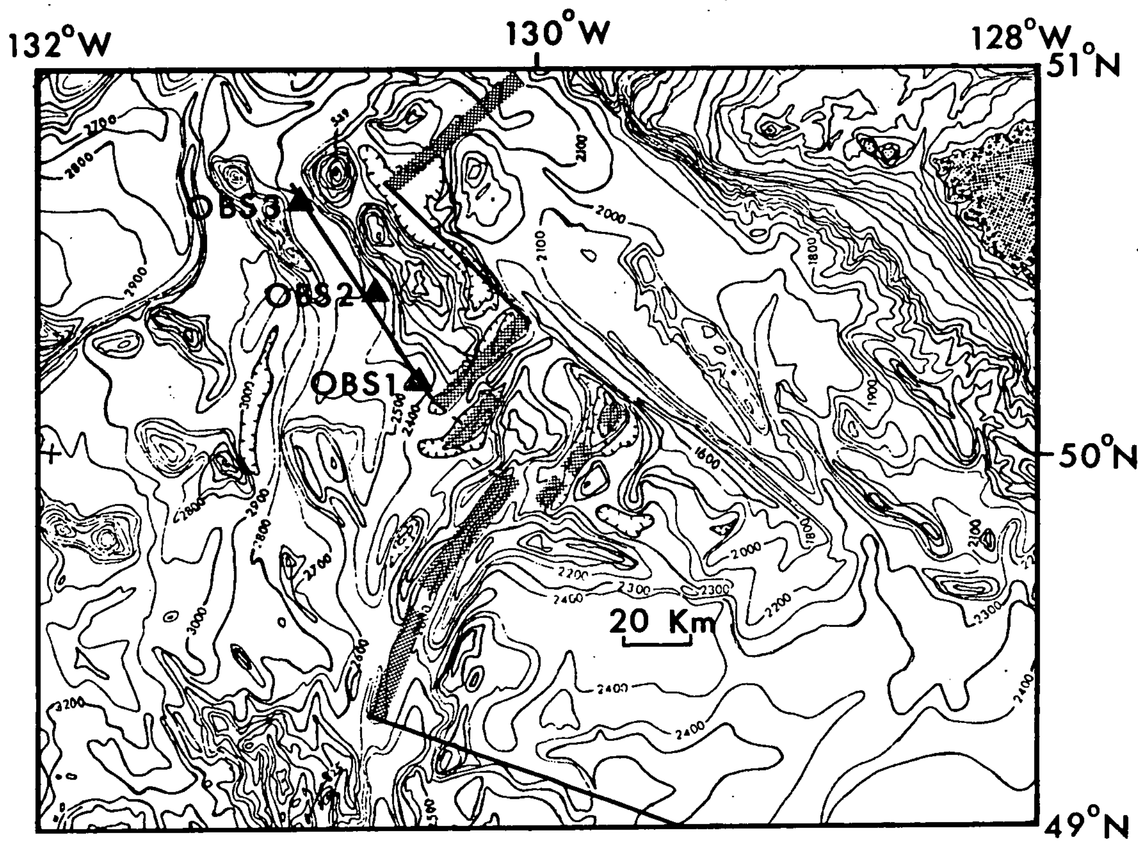

Figure 1.3 Location of the three OBS's and the seismic refraction profile off Explorer ridge. The interpreted ridge areas are stippled. Bathymetric contours are in meters (from Tiffin and Seemann,1975).

The Revere-Dellwood fracture zone is a topographic low extending northwest from the ridge. The seismic refraction profile which forms the basis of this study is located approximately parallel to this fracture zone, on the Pacific plate, and is separated from the transform fault by a series of seamounts. Figure 1.3 shows the locations of the three OBS's and the 80 km line along which explosives were detonated.

Other than the work of Malecek and Clowes (1978), centred at 49°30' and 130°W on Explorer plate, no detailed geophysical study in the region of Explorer ridge has been published. The present OBS experiment extends seismic refraction coverage to the northwest from the ridge. Hyndman et al. (1978) have given a preliminary interpretation of these data.

1.2 Outline of study :

The geophysical experiments carried out on the cruise in the summer of 1976 can be divided into four aspects; namely deep crustal seismic sounding, a seismicity study, heat flux measurements and continuous seismic profiling. The concern of this study is the deep crustal seismic sounding survey. Hyndman et al. (1978) have presented a simple interpretation based on the conventional layered model using first arrival travel times. Current and more sophisticated interpretation techniques (Kennett,1977) use travel times of all observable phases as well as amplitude information. Such methods yield a more realistic velocity-depth model of the oceanic crust. As well, one of the main reasons for using OBS's instead of the more traditional hydrophone or sonobuoy systems is the desire to obtain accurate information on both the P-wave and the S-wave velocity structures by using 3-component recordings. Then, Poisson's ratio can be estimated and this leads to speculation concerning the geological properties and origin of the oceanic crust.

The following is a brief description of procedures used in processing and interpreting the data. Details are given in subsequent chapters. The original seismograms recorded on slow speed, direct mode tape recorders had to be transcribed to FM tape for subsequent digitization. Time and amplitude corrections are applied to account for water and sediment thickness variations and different charge sizes. Travel time information is derived from record sections and then inverted, using the tau inversion technique of Bessonova et al. (1974,1976), to give an envelope of all possible velocity-depth models consistent with the travel times for both P and S waves. A linearized inversion technique described by Johnson and Gilbert (1972) is further employed to give a best fit model for the travel time data. Finally the travel time and amplitude content of the data are incorporated into an interpretation using disk ray theory synthetic seismograms (Wiggins,1976). With this procedure, the aim is to obtain a detailed seismic model of the crust and upper mantle in the region immediately northwest of Explorer ridge.

2. DATA ACQUISTION AND PRELIMINARY PROCESSING

2.1 Instrumentation :

Four OBS's of two different types (two units of each type) were used in this study. Hyndman et al. (1978) have already described the field procedure for this experiment. For completeness, I will outline briefly the instruments and field operations.

Both types of instruments used are of the free-fall, pop-up class. The first type, designed by the University of Washington (Lister and Lewis,1976; Johnson et al.,1977) hereafter is referred to as the PGC instrument; the second type, developed by the Hawaii Institute of Geophysics (designated as POBS by Sutton et al.,1977) has a release mechanism modified by Heffler and Locke (1977) and is referred to as the AGC instrument. Each design differed completely in shape, size and instrumentation. Only the recording aspect is of immediate concern in this study.

Both instruments record in continuous direct AM mode using a 4 channel tape head. The PGC instrument (see Figure 2.1) records signals at a tape speed of 1 mm sec^{-1} from one vertical and two horizontal 4-1/2 hz geophones with a 20 hz time code in the first channel. The overall frequency response is bandlimited between 2 hz and 100 hz. Signal compression by a bipolar square-rooting circuit increases the dynamic range to 80 db. The AGC instrument records signals at a tape speed of 0.46 mm sec^{-1}, and has a dynamic range of

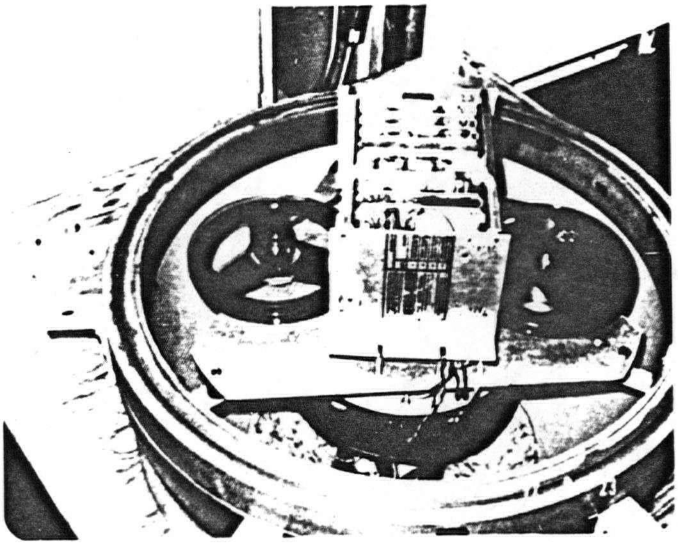

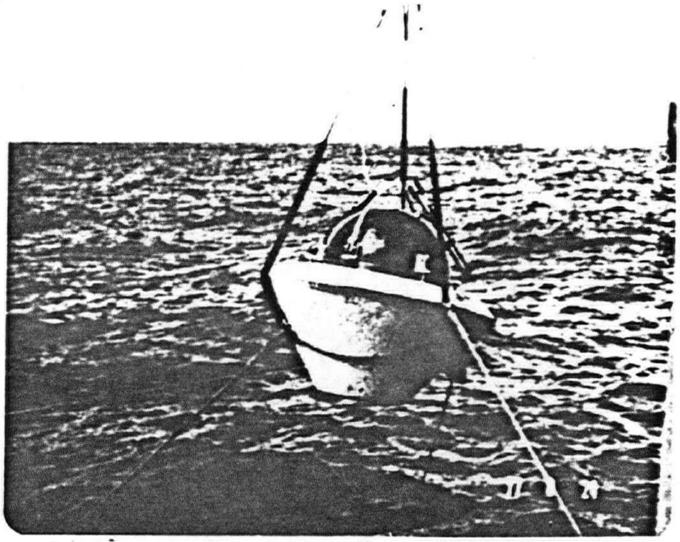

Figure 2.1 OBS system (PGC instrument)

(a) Photograph of recording electronics in the lower hemisphere of the spherical housing. The tape transport and electronics are in the upper part. Batteries and the three geophones are below.

(b) Launching of an OBS. The sphere containing the instrumentation is attached to a specially designed concrete anchor for deployment. At a predetermined time, the sphere having positive buoyancy releases from the anchor and floats to the surface.

40 db and a bandwidth of 2 hz to 20 hz. To detect the direct water wave arrival, the high frequency output of the hydrophone is rectified into the time channel. Signals are recorded through one hydrophone and one vertical and one horizontal 4-1/2 hz geophones.

2.2 Field data collection :

The four OBS's were deployed along an 80 km profile perpendicular to the northern end of Explorer ridge and parallel to Revere-Dellwood fracture zone. Position accuracy of about 1 km is attained by the use of satellite and Loran A navigation. Two PGC instruments (designated OBS1 and OBS2) were launched about 5 km and 35 km from the ridge axis, in crust around 0.2 m.y. and 1.2 m.y. old. The two AGC instruments (designated OBS3 and OBS4) were deployed close together about 75 km and 79 km from the ridge axis, in crust around 2.5 m.y. old. Unfortunately OBS4 failed to return and was lost. Figure 1.3 shows the locations of the three recovered OBS's and the seismic refraction profile.

While cruising at a speed of 4.32 m sec^{-1} (8.4 kt), 2300 kg of high velocity explosives were detonated in 81 alternating large and small shots ranging from 4.5 kg to 180 kg in size. This shooting pattern was designed with the expectation that the large charges provide sufficient energy to distant OBS's whereas the smaller charges would not overload the OBS's nearby. The charges were all time-fuse detonated at predetermined optimal depths (Shor,1963) assuming a constant sinking rate of 1 m sec^{-1}. The ditch time (time from dropping of charge overboard until detonation) was noted. Direct water wave arrivals, detected with a towed hydrophone and a low sensitivity geophone on the ship's deck, and the WWVB radio time code were recorded on FM tape. As well, a high speed two-channel chart recorder was used to monitor the direct water wave arrivals and WWVB. All shots were recorded on the three OBS's, resulting in one reversed profile (OBS1 and OBS3) and two split-spread profiles (OBS2, leg1 and leg2) which overlapped the longer ones. The profile OBS2 leg1 is the northwest trending line to OBS3 and the profile OBS2 leg2 is the corresponding southeast trending line to OBS1.

In addition to the explosive charges, a 16 litre (1000 cu in) airgun was employed to run 30 km profiles over each OBS site in direction along and across the line. Interpretation of these data is beyond the scope of this study.

2.3 Digitization and demultiplexing :

The data set for this project was originally recorded in direct continuous AM mode (see section 2.1). A method to transcribe the data into digital form is essential and the treatment used depends on the initial recording instruments (types PGC and AGC) since the recording speed of each is different. The only analog playback system currently available was a Hewlett-Packard Model 3960 tape recorder. Its slowest playback speed of 15/16 ips, representing a real time speed up of about 24 times, gives a time base which is beyond the present analog-to-digital conversion capability of the marine digital acquisition system in the department (Clowes,1977). In order to circumvent this difficulty, a two-stage procedure of playback and recording was followed.

For the PGC instruments, the data is first transcribed from AM to FM at a playback speed of 15/16 ips (approximately 24 times real time) and a recording speed of 15 ips. The FM tape was then replayed at a speed of 15/16 ips, resulting in an overall change of 1.5 times real time, for digitization at a rate of 312.5 samples sec^{-1}. This gives a Nyquist frequency of 104.5 hz in real time. The equivalent real time sampling rate of about 0.0048 sec just barely avoids possible aliasing problems associated with the 80 hz high cut (24 db oct^{-1} rolloff) analog filter employed. Thus, it is recommended that a lower corner frequency for the high cut analcg filter should be used, but the real-time digitization rate of 209 samples sec^{-1} is adequate for interpretive purposes.

The data tape of the AGC instrument was transcribed to FM mode at a playback speed of 16 times real time and a recording speed of 15 ips by Mr. D. L. Barrett of the Atlantic Geoscience Centre. Replaying the FM tape at a speed of 15/16 ips, resulting in a final rate of 1.0 times real time, and digitizing at a rate of 312.5 samples sec^{-1} gives a Nyquist frequency of 156 hz in real time. No analog aliasing filter is applied as the data are originally bandlimited between 2 hz and 20 hz.

All the data tapes from the PGC and AGC instruments are edited before digitization. Overall, the data recorded by the PGC instruments are of higher quality than the AGC instruments both in terms of lower ambient noise and a less severe reverberation problem. The records are digitized from roughly 5 seconds before the first arrival to about 5 seconds after the direct water waves. The digital tapes are then demultiplexed and written on new tapes. Figure 2.2 shows some examples of the raw data. It displays significant reverberation after the onset of the first arrival, a phenomenon common to many OBS seismograms. This particular problem will be considered further in Chapter 3.

2.4 Time determination and correction :

Once the data are edited, digitized and demultiplexed, the next logical procedure is to compile seismograms into a record section. Before proceeding to this stage, accurate origin time determination are required. As mentioned in section 2.1, direct water wave arrivals are recorded along with the WWVB signal aboard the ship. Assuming a charge sinking rate of 1 m sec^{-1} for the measured ditch time, a mean ship speed of 4.32 m sec^{-1} (8.4 kt), and a water velocity of 1.49 km sec^{-1}, the correct origin time of each shot can be extrapolated using the slant path approximation. By assuming a vertical ray travel path, all shots are time corrected to be at the sea's surface. The estimated error of this static correction is about 15 msec.

Corrections for seabottom topography and sediment

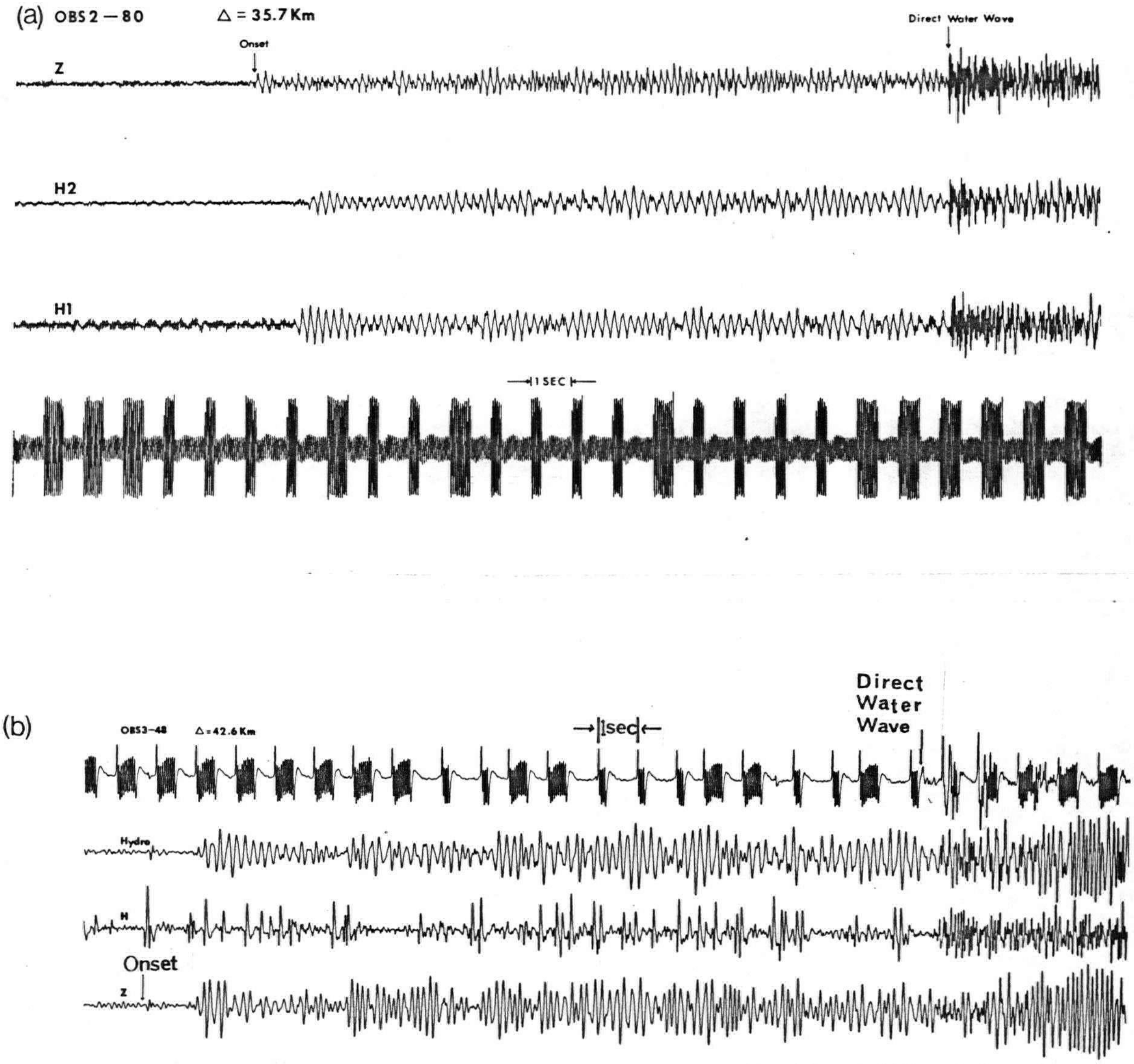

Figure 2.2 Examples of demultiplexed digital data plotted on a Calcomp plotter. Note the reverberations inherent in the OBS coda after the onset of the first arrival.

(a) PGC instrument.

(b) AGC instrument.

thicknesses are made by taking a reference water depth of 1.74 sec (1-way time), a sediment thickness of 0.18 sec (1-way time) and assuming a deep refractor (layer 3) of 6.3 km sec^{-1}. Differences from these reference values are replaced by 4.5 km sec^{-1} material (layer 2) using a refracted path approximation. The 4.5 km sec^{-1} material and the 6.3 km sec^{-1} refractor are chosen from preliminary results of Hyndman et al. (1978). Water depth and sediment thickness are estimated from a high resolution pulser profile along the refraction line (see Figure 2.3) using a constant water velocity of 1.49 km sec^{-1} and an assumed average P-wave sediment velocity of 1.8 km sec^{-1} (Peterson et al.,1974). This correction contributes an additional error of up to 10 msec. Since the OBS clocks were all synchronized with a standard clock before deployment, an estimate of the clock drift can be made by comparison with the same standard clock after recovery. Error for this clock drift correction is less than 25 msec over the recording period for the refraction program. Thus, the overall total travel time error is estimated to be a maximum of 50 msec.

2.5 Amplitude correction :

Amplitude information is useful as a discriminant for refining velocity models, since travel time data alone, as will be seen in Chapter 4, will give rise to many possible velocity-depth curves. Thus, it is necessary to recover the original amplitude information and compensate for the effect of instrument response, varying charge size and geometrical

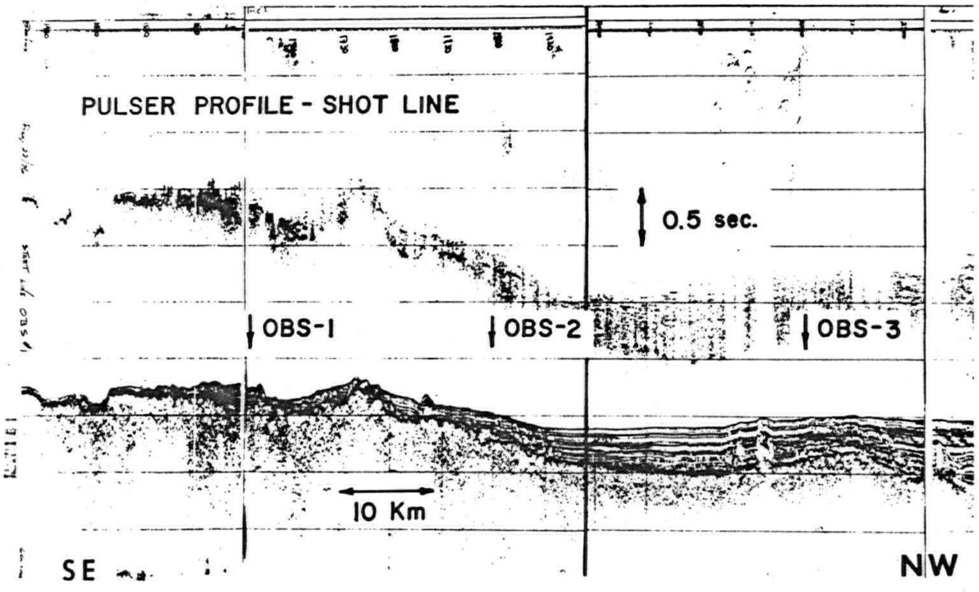

Figure 2.3 Topography and sediment structure along the refraction profile.

spreading effects.

In section 2.1, it was mentioned that the PGC instruments use a bipolar square-rooting circuit to improve the dynamic range of the recording system. The first step undertaken to recover the original signals of OBS1 and OBS2 is simply to apply a squaring filter. This poses no difficulty as the data are stored in digital form and the unity level for squaring has a low value (~15mv) as determined by calibration signals. For data from OBS3, this step is not necessary. To compensate for charge size variations, the $W^{2/3}$ relationship between charge size (W in lbs) and seismic amplitudes determined experimentally by O'Brien (1967) is applied. That is, every trace of the OBS's is multiplied by a factor $W^{-2/3}$.

Compensation for the geometrical spreading effect is based on the theoretical results of Červený and Ravindra (1971, p147) that head wave amplitudes decrease as $1/r^2$ at large distance r. Although wide angle reflection amplitudes vary as $1/r$ (Braile and Smith,1975) and amplitude decreases near the critical distance is of the order of $1/r^3$ or $1/r^4$, a factor of r^2 is used on all real and synthetic seismograms. This provides good amplitude normalization along the profile, enabling arrivals at all distances to be seen clearly.

2.6 Shot to OBS distances :

The final information needed in compiling a record section is the determination of the shot-to-OBS distances. This information was compiled for the preliminary interpretation of Hyndman et al. (1978). Dr. Hyndman provided all distances used here. For completeness, I will give a summary of the procedures employed. All direct water wave arrivals and their multiples, corresponding to different travel path segments through the water, are identified. Then, ray tracing and synthetic seismograms as described by McMechan (1978) are employed to give a travel time - distance relation for each path using an empirically determined water velocity versus depth profile in the area. Finally, the constraint that the computed distances between different shots and different OBS's should be consistent was used as a check on these distances, giving an accuracy of about 0.3 km.

3. DATA ANALYSIS AND RECORD SECTIONS

3.1 Reverberation problem :

Reverberations and bubble pulses are inherent problems associated with many marine seismic studies. In particular, SV waves trapped in the sediment layer have proven to be the dominant factor affecting seismograms recorded by OBS's (Lewis and McClain,1977). This makes picking secondary arrivals extremely difficult. In this section, I will discuss some initial attempts made toward dereverberation of the OBS seismograms.

Figure 3.3a on page 31 shows a typical trace of recorded data. The reverberation stands out clearly. Note that the nonlinearities in the waveforms are due solely to the bipolar square-root filter in the OBS itself. After being processed through an inverse squaring operator to recover the original signal levels, a digital bandpass filter was applied to the

Location	Sediment thickness (m)	RF observed (hz)
OBS1	99 ± 9	6.98 ± 0.60
OBS2	225 ± 9	7.38 ± 1.69
OBS3	315 ± 9	7.20 ± 1.06

TABLE 3.1

Reverberation frequency as a function of sediment thickness.

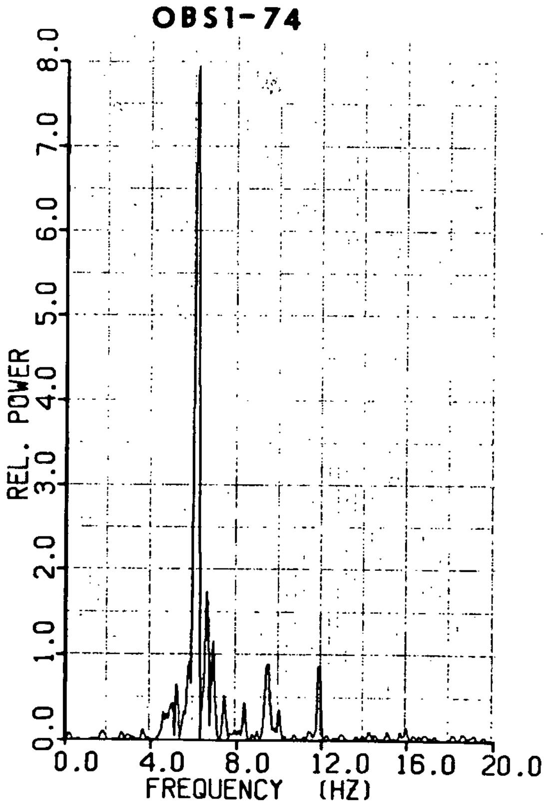

Figure 3.1

A typical power spectrum of a seismic trace from OBS1. This spectrum is computed for the time interval from 0.25 sec before to 9 sec after the first arrival. The shot was directly over the OBS (Δ=0 km).

data as a first step in data enhancement. Numerical experiments using different bandwidths were tested. Corner frequencies at 5 hz and 20 hz were found to yield the best results even though considerable ringing still persisted after filtering. (see Figure 3.3b).

Inspection of the individual power spectrum of a number of seismograms at each site shows that most of the energy is concentrated near one frequency. Figure 3.1 shows a typical power spectrum from OBS1. The frequency at which this peak occurs will henceforth be referred to as the reverberation frequency (RF). A statistical analysis of these RF's has been done on all of the recorded seismograms. As well, the inferred sediment thickness corresponding to each OBS site was derived from the pulser profile (Figure 2.3) by assuming a constant P-wave sediment velocity of 1.8 km sec^{-1}. A comparison between the RF's and the sediment thickness under each OBS location is made in Table 3.1. Since the average RF's corresponding to the three OBS locations have standard deviations which overlap, no direct relationship is inferred. However, this analysis does show that the reverberation associated with many OBS seismograms probably has a more complex origin than the suggestion of an SV wave trapped in a sediment layer.

The monochromatic signature of the power spectrum suggests that dereverberation might be accomplished by using a zero phase shift, frequency rejection filter (Kanasewich, 1975). The filter is tuned at a frequency corresponding to the RF of each seismogram with adjustments on the degree of notch or sharpness. Figure 3.3b,c displays a typical trace before and after it has been processed by the notch filter. Significant decrease in the reverberation is observed and the seismic character of the trace is improved. But the identification of secondary arrivals remains extremely difficult.

3.2 REMODE filter :

Another approach to enhancing S-wave arrivals and minimizing the reverberations is to use a polarization filter. Two types of such filters are reported in the literature. However, they are both based on the principle that P and SV motions are rectilinearly polarized and thus may be enhanced relative to the signal generated noise and random background noise. As well, both types are time-varying, non-linear filters. The first class of polarization filter reported in this section is the REMODE (REctilinear MOtion DEtector) type originally developed by the Teledyne research group (Sax and Mims, 1965; Griffin, 1966a,b; Sax, 1966).

Consider the vertical z(t) and the radial r(t) seismograms as simple unit-amplitude sinusoids with no phase difference (ie. pure rectilinear motion). The cross correlation function G(T) with a lag T between z(t) and r(t) for a window length w centered at time t is expressed as

$$G(T) = \int_{t-w/2}^{t+w/2} \sin(t)\sin(t+T)\,dt \qquad (3.2\text{-}1)$$

which after integration reduces to

$$G(T) = \frac{1}{2}\left\{\sin(w)\sin(2t)\right\}\sin(T) + \frac{1}{2}\left\{w - \sin(w)\cos(2t)\right\}\cos(T) \qquad (3.2\text{-}2)$$

If w is large compared to unity, then

$$G(T) \approx \frac{w}{2}\cos(T) \qquad (3.2\text{-}3)$$

which is an even function. By the same token, if z(t) and r(t) have a phase lag of 90° (ie. pure circular motion), and again if w is large compared to unity, one arrives at the relation

$$G(T) \approx -\frac{w}{2}\sin(T) \qquad (3.2\text{-}4)$$

which is an odd function.

Thus, the even part of G(T) can be used as a filter function to convolve with the original time series (Sax and Mims,1965). The even part is used because generally the seismograms involved are contaminated with random noise and so rectilinear detection will be a better discriminator. This type of filter is both amplitude and phase dependent with respect to the recorded signal. To eliminate the amplitude dependence, the filter function is multiplied by a normalisation factor defined as the square root of the product between the autocorrelations of z(t) and r(t). The phase dependence is inherent and cannot be removed. The resultant filter is referred to as REMODE 3 by Griffin (1966a).

For pure compressional motion, the particle trajectory would follow the E1 component of Figure 3.2c and for pure transverse (SV) motion, the particle motion would follow the corresponding E2 component. Thus, the REMODE 3 filter can be shaped to a P-detection filter (designated REMODE 3A by Griffin,1966a) or an S-detection filter (designated REMODE 3B here) by setting the product of $z(t)r(t)$ to zero using this 'particle-motion' criteria such that

$$z(t)r(t) \geq 0 \text{ for P-detection (REMODE 3A) filter}$$

and $$z(t)r(t) < 0 \text{ for S-detection (REMODE 3B) filter.}$$

Basham (1967) successfully applied a REMODE 3A filter to land-recorded, P-wave codas as an aid in the identification of different phases of P-arrivals. Yet to my knowledge, no attempt at using a REMODE-3B filter on marine seismic data as an aid in the identification of S-wave arrivals has been published. This fact and the importance of identifying S-wave arrivals provided much of the impetus to explore the feasibility of using REMODE 3B filters as an interpretation aid for OBS data (see section 3.4).

3.3 Principal component analysis :

In this section, I will discuss the type of time-varying filter introduced by Flinn (1965) and modified by Montalbetti and Kanasewich (1970). Following Souriau and Veinante (1975), a two-dimensional analysis is given here. For convenience, this type of filter is hereafter referred to as COMA2D (2-Dimensional COMponent Analysis) filter.

Assume for simplicity that two orthogonal seismometers are oriented in a fashion such that one is parallel to the SV particle motion and the other is parallel to the P motion. In this way, the covariance matrix

$$M = \begin{bmatrix} DP & CX \\ CX & DS \end{bmatrix} \tag{3.3-1}$$

for a set of N observations taken over the two seismograms will have a simple geometrical interpretation in Euclidian vector space. In equation 3.3-1, DP and DS are the corresponding variances of the seismogram-recorded P and SV motion, while CX is the covariance between DP and DS. The eigenvalues of M are

$$l1 = (DP + DS + d)/2$$

and

$$l2 = (DP + DS - d)/2 \tag{3.3-2}$$

in which $d = \{(DP-DS)^2 + 4CX^2\}^{1/2}$

such that $l1 \geq l2 \geq 0.$

The corresponding normalized eigenvectors are

$$x1 = (\cos a, \cos b)$$
$$x2 = (-\cos b, \cos a) \tag{3.3-3}$$

The components are simply direction cosines between the vectors and the direction of a rotated seismogram such that

$$\cos^2 a = (DP - DS + d)/2d$$
$$\cos^2 b = (DS - DP + d)/2d \tag{3.3-4}$$

In terms of Euclidian geometric space, x1 and x2 are in the direction of the major and the minor axis of an ellipse with lengths equal to the square-roots of the eigenvalues. For pure rectilinear motion, l2 is close to zero while for pure circular motion I2 approaches the value of I1. Thus the filter function

$$F1(t) = 1 - I2/I1$$

would enhance all rectilinear motion. But one can further shape the COMA2D filter into a P-detection or a S-detection filter by cascading the filter function F1(t) with another direction-oriented function

$$F2(t) = \cos b \quad \text{for P-detection filter}$$

or $$F3(t) = \cos a \quad \text{for S-detection filter.}$$

The filter functions F1(t), F2(t) or F3(t) are all taken over a specific time window w, similar to the REMODE filter, and these are then used as point by point gain controls on the original time series. But first, these filter functions are all smoothed in a smaller window in order to subdue any anomalous spikes (Montalbetti and Kanasewich,1976).

This kind of time-varying, nonlinear filter has been applied on land seismic data (Flinn,1965; Montalbetti and Kanasewich,1970; Souriau and Veinante,1975; Spence,1976) with promising results but no work has yet been published on marine seismic data.

3.4 Application to data :

The seismograms have to be rotated before the application of the REMODE and the COMA2D filters. Since all OBS's used (both PGC and AGC instruments) are of the free-fall pop-up class, orientation of the horizontal seismometers is not known and must be determined. First, the mean azimuthal angles of approach (α) of the seismic energy with respect to one of the horizontal components are determined using the relative amplitudes of the two horizontal seismograms over one and a half cycles of the direct P-wave arrivals. Second, the two horizontal seismograms are then resolved into the radial and the transverse components (see Figure 3.2a). Third, the angle of incidence of the seismic ray (β) is found from a particle motion plot (between the radial and the vertical components) using one and a half cycles of the direct P-wave arrivals. Fourth, the radial and the vertical components are further rotated into two orthogonal components C1 and C2 or E1 and E2 (see Figure 3.2b,c). The rotation to C1 and C2 is required before the application of the REMODE filter since C1 and C2 are both 45° apart from the angle of incidence and so share approximately equal energy. Thus the even part of the cross correlation function G(T) between C1 and C2 would be maximized (see section 3.2). On the other hand, the rotation to E1 and E2 facilitates the application of the COMA2D filter as they are separately parallel to the direction of the P and SV particle motions.

Table 3.2 tabulates the angles α and β used for rotation of all the seismograms. The values shown are based on a statistical analysis done on all the particle motion plots from each individual seismogram. Since the AGC instrument has only one horizontal geophone, it is taken as the radial component to be used in determining the angle β. Both tabulated angles α and β are believed to be as accurate as

(a) about vertical component : α is the azimuthal angle of approach.

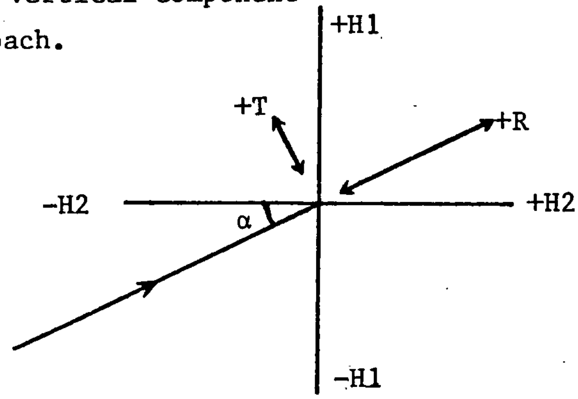

(b) about transverse component (for REMODE filter) : β is the angle of incidence.

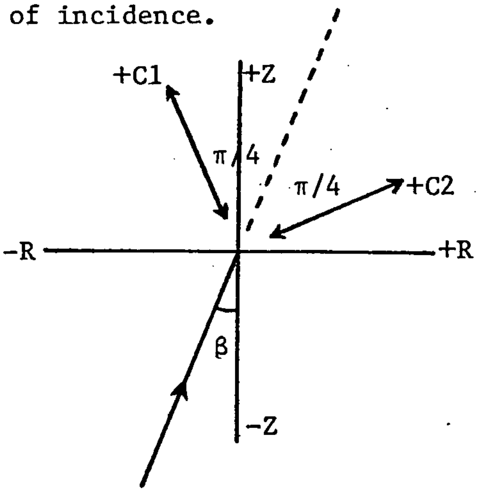

(c) about transverse component (for COMA2D filter) : β is the angle of incidence.

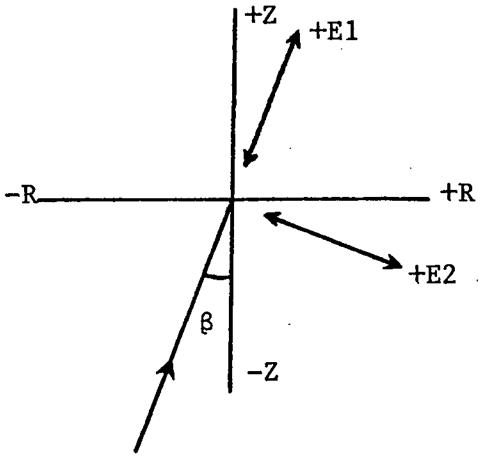

Figure 3.2 Seismogram rotation diagrams.

possible with the given data and are consistent with the relative amplitudes of the 3-component seismograms. However, an analysis using the preliminary layered velocity-depth model of Hyndman et al. (1978) shows that β should be in the range of 13° to 24°. Only OBS2 has β lying within this range and even allowing for large variations in β determined from a layered model, the β's of OBS1 and OBS3 are anomalous with respect to the expected value. Part of the discrepancy may be due to the data analysis procedures, especially for OBS3 in which the horizontal component was taken as the radial component. Another reason for the differences probably involves near-surface inhomogeneities which would distort the upgoing ray paths.

After the seismograms have been rotated, the optimal parameters for the filters must be determined. After some numerical experiments, a window length of half a second was chosen for both the REMODE and the COMA2D filters. The time

Location	Alpha (deg)	Beta (deg)
OBS1	42.6 ± 2.99	51.3 ± 3.08
OBS2	44.3 ± 3.05	17.0 ± 2.22
OBS3		63.4 ± 3.29

TABLE 3.2

Angles alpha and beta from particle motion analysis.

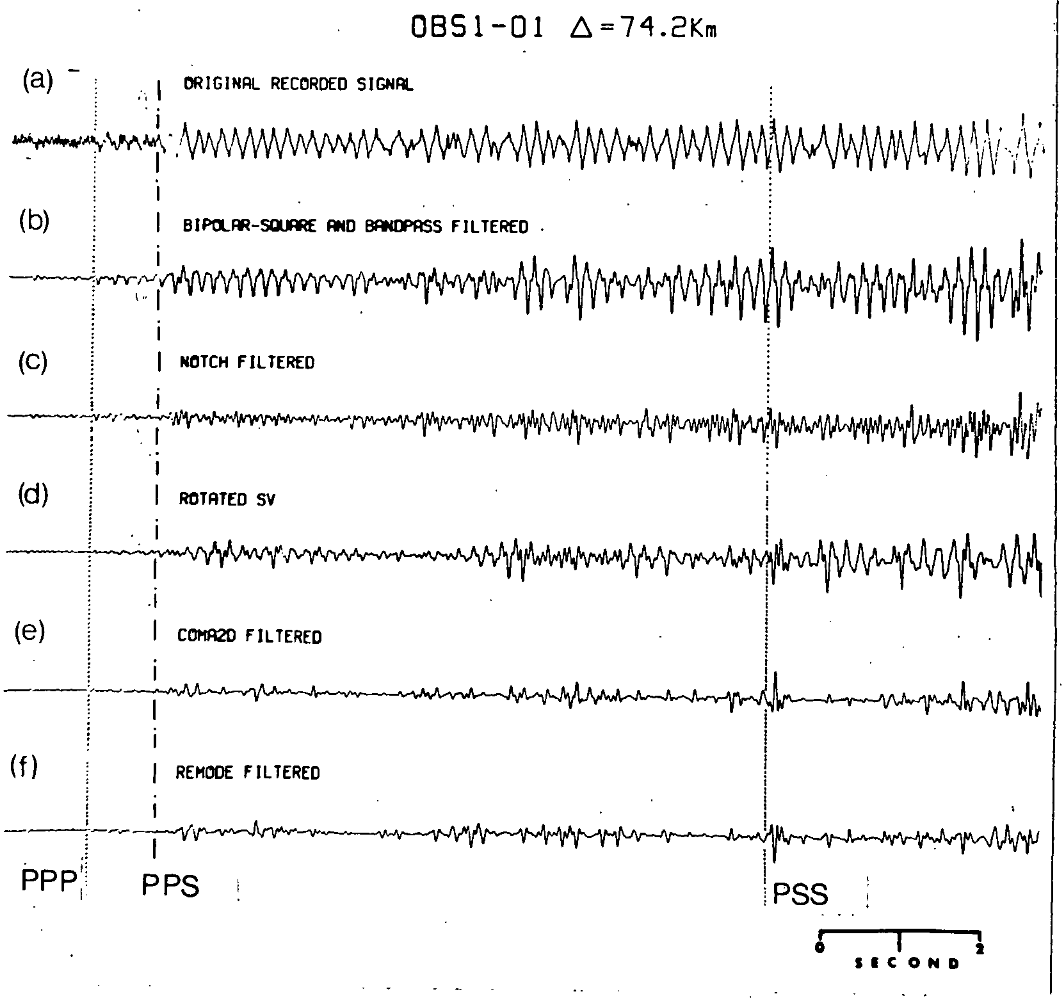

Figure 3.3 Seismic signals before and after filtering. Amplitude for each trace is scaled arbitrarily for display purposes.

(a) Original recorded signal.

(b) Bipolar-square and bandpass filtered.

(c) Notch filtered with a notch at 6.3 hz.

(d) Rotated SV component.

(e) COMA2D filtered.

(f) REMODE filtered.

lag used for the cross correlation in the REMODE filter and the smoothing window used for the filter functions (see section 3.3) in the COMA2D filter are found to yield best results if they are set at one-third of a second. Figure 3.3 displays a typical trace before and after it has been processed by the REMODE (3.3f) and the COMA2D (3.3e) filters.

Both filters have reduced the reverberation considerably, with an accompanying tradeoff of lower signal-to-noise ratio. However, the enhancement of the PSS phase (refracted S-wave) is quite distinct. The reason for the phase difference of 180° observed between the different filtered traces is uncertain but may be due to the analysis program. In general, based on a number of trials on different seismograms at different epicentral distances, results (not shown) from the COMA2D filter are more encouraging than the REMODE filter.

Figure 3.4 shows portions of a COMA2D filtered record section of OBS1 data. This section can be compared with the rotated SV component record section as shown in Figure 3.9. A single trace comparison is given in Figure 3.3d,e. In general, the rotated SV component data display a larger reverberation characteristic while the COMA2D filtered section is more spiky. Because of this, the signal-to-noise ratio on the rotated SV data is considerably higher. For OBS2, the rotated SV record sections showed clear PSS arrivals so additional filtering was unnecessary. However, for OBS1, timing of the PSS phase required the combined use of both types of sections, especially for the larger distances.

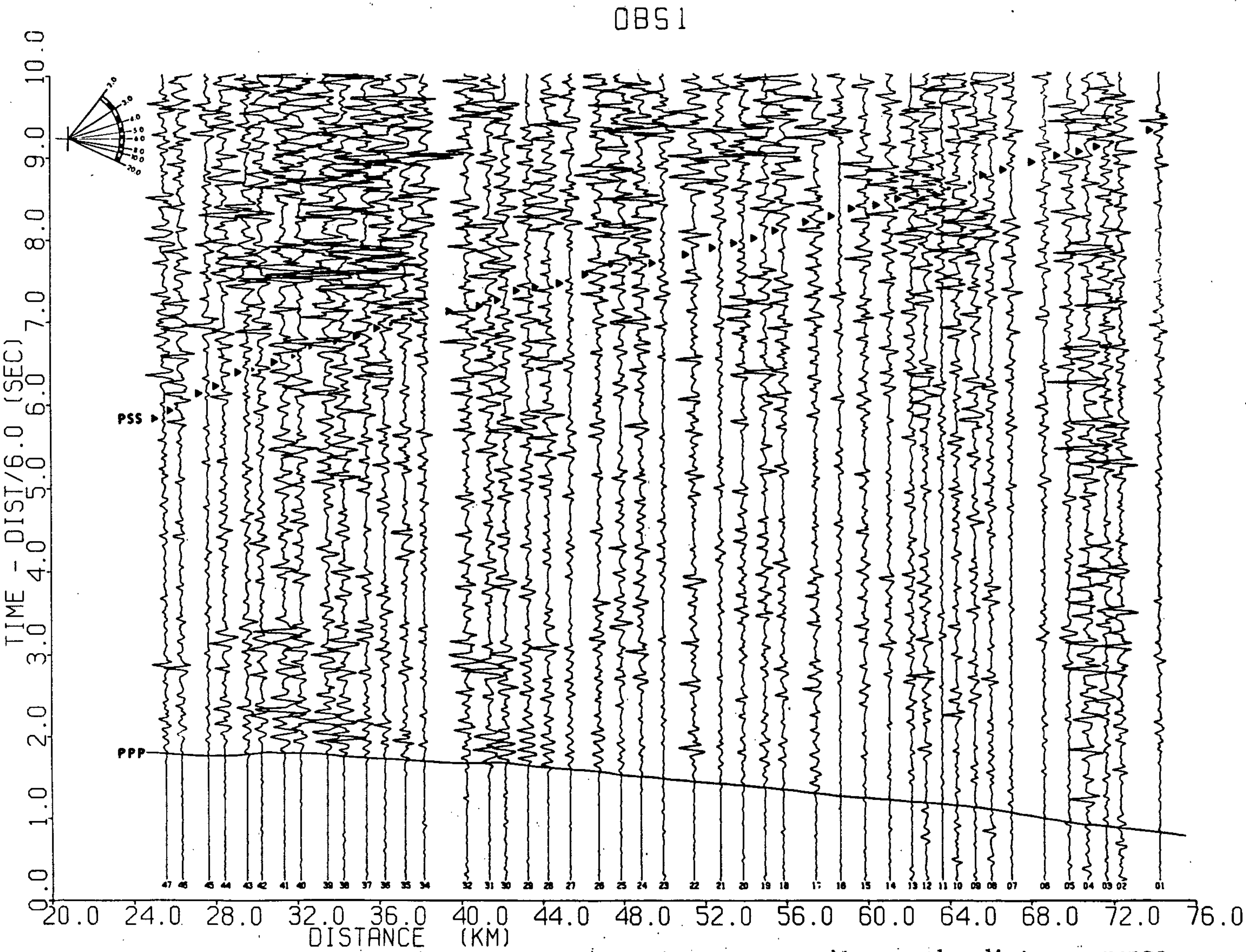

Figure 3.4 COMA2D filtered record section of OBS1 (SV component) over the distance range 25–75 km. The data are also bandpass filtered from 5 to 20 hz. PPP line is transposed from Figure 3.5. PSS picks shown by triangles are made using this section and that of Figure 3.9.

3.5 Record sections :

Figures 3.5 to 3.8 are vertical component, bandpass filtered record sections compiled from the seismograms recorded by each OBS. Both the PPP phase (refracted P-wave), and the PPS phase (converted S-wave at the sediment-basement interface) are shown. The PSS phase (refracted S-wave) appears in the rotated SV component, bandpass filtered record sections displayed in Figures 3.9 to 3.12. Note that the PPP arrivals shown in Figures 3.5 to 3.8 are simply overlain onto the SV component sections. All seismic traces shown in these figures are both statics corrected and amplitude compensated as discussed in sections 2.4 and 2.5. Timing errors of the PPP and the PSS phases are estimated to be 10 and 50 msec, respectively. These errors, plus the error of 50 msec associated with the timing corrections (see section 2.4), are used in the tau and linearized inversion schemes.

The onset of arrivals in OBS3 (Figure 3.8) could be picked confidently only to a distance of 40 km. Times for distances greater than 40 km are determined using the constant, observed interval time of 1.15 sec between the PPP and the PPS phases, and the capability of identifying the latter arrivals. Due to the more severe inherent instrumental reverberation problem of OBS3 (AGC instrument), the travel time branch of the refracted S-wave is masked (see Figure 3.12).

The irregular trend of the onset of the PPP arrivals in

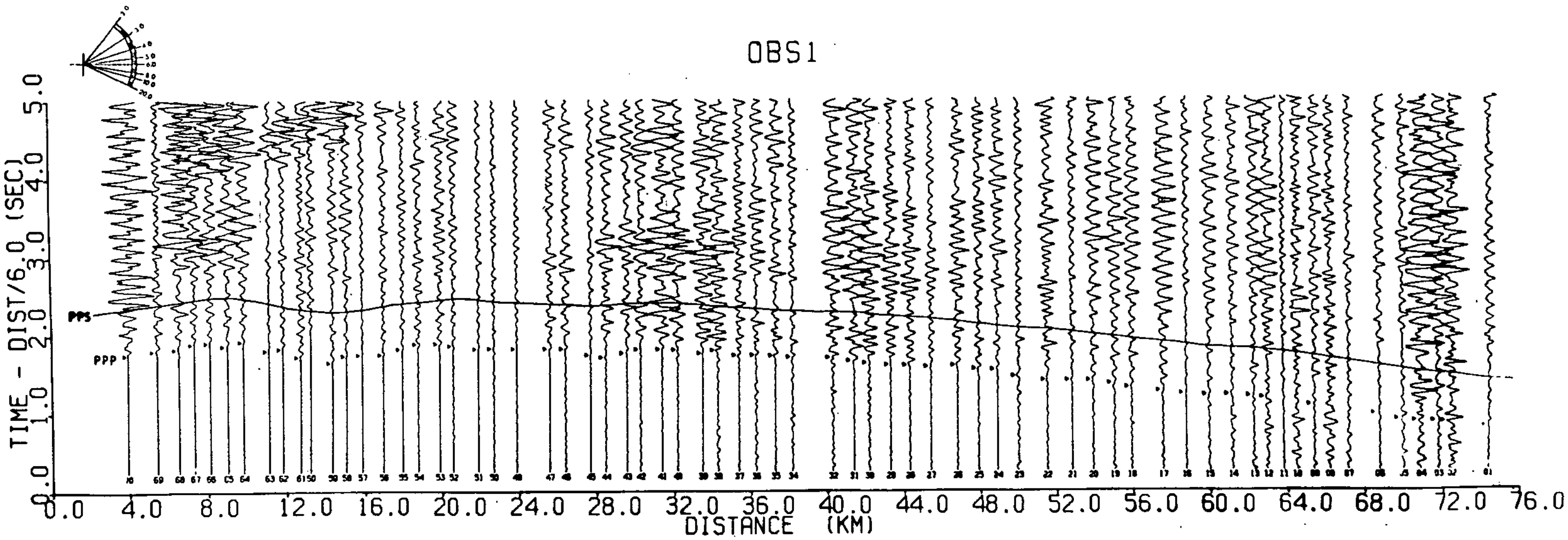

Figure 3.5 Vertical component bandpass filtered (5-20 hz) record section of OBS1. Amplitude corrections, outlined in section 2.5, have been applied. Solid triangles show first arrival picks made from this section and from an unfiltered section (not shown). The line shows the PPS phase identified on the SV component section (Figure 3.9).

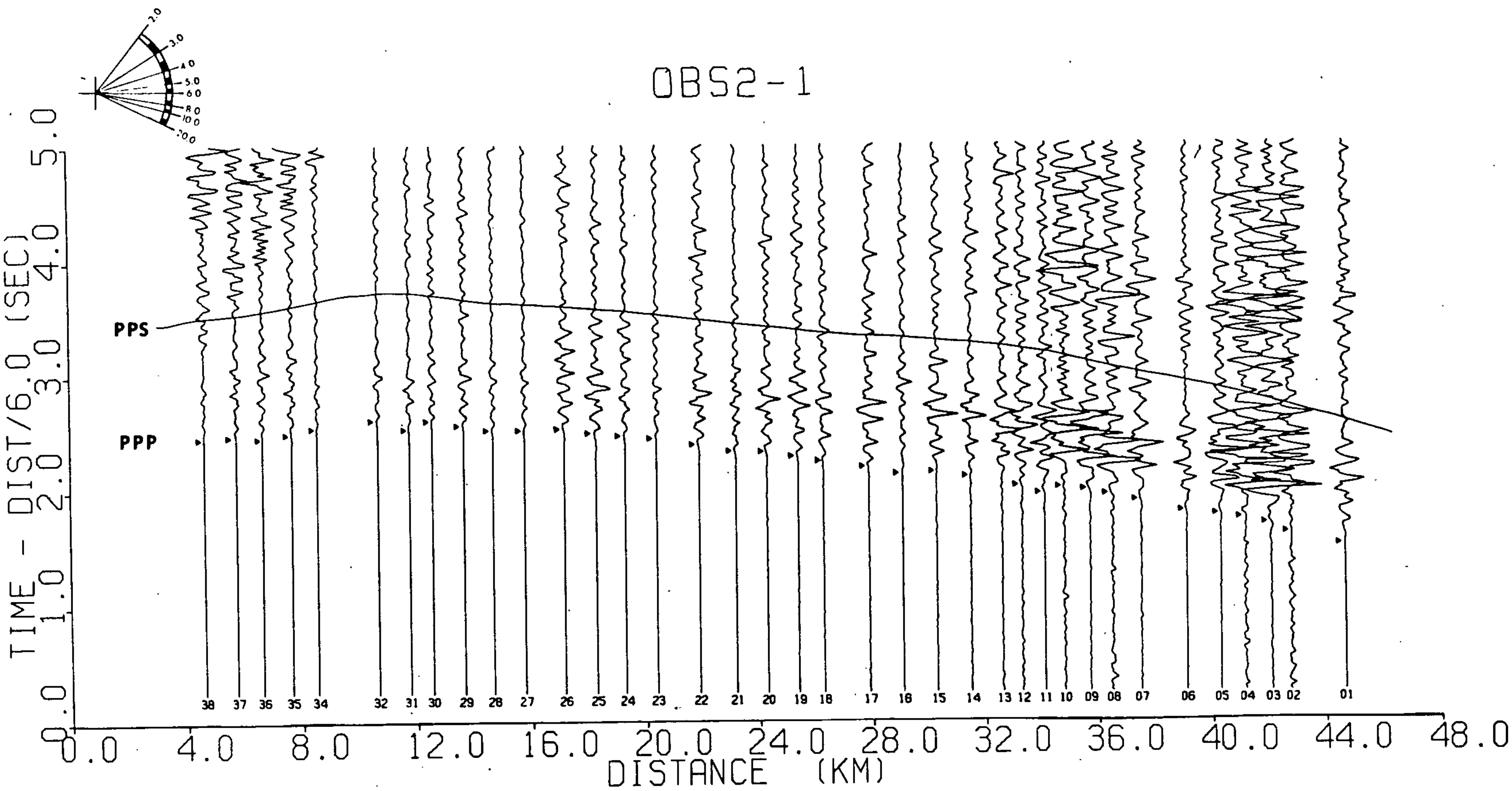

Figure 3.6 Vertical component bandpass filtered (5-20 hz) record section of OBS2 leg 1. Amplitude corrections, outlined in section 2.5, have been applied. Solid triangles show first arrival picks made from this section and from an unfiltered section (not shown). The line shows the PPS phase identified on the SV component section (Figure 3.10).

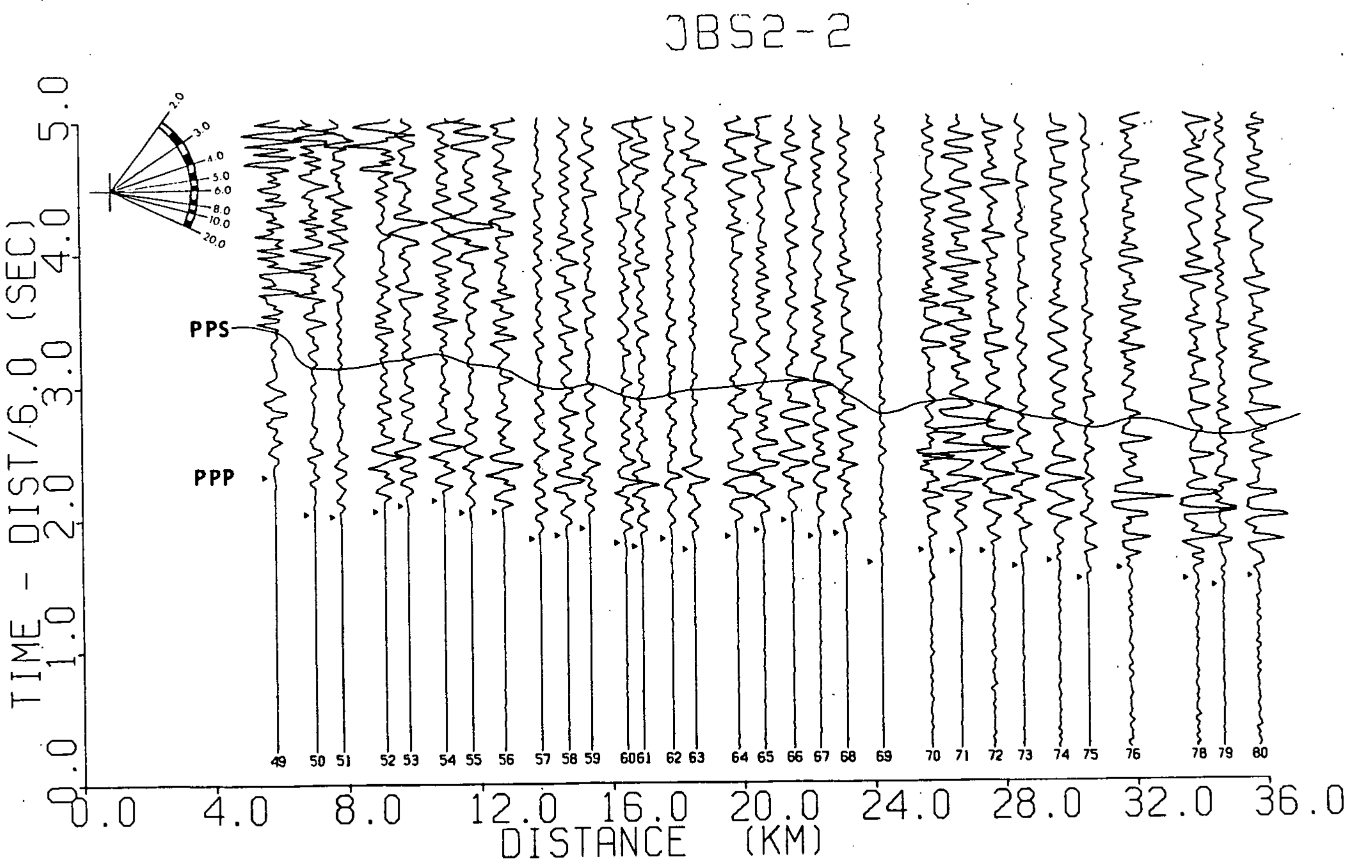

Figure 3.7 Vertical component bandpass filtered (5-20 hz) record section of OBS2 leg 2. Amplitude corrections, outlined in section 2.5, have been applied. Solid triangles show first arrival picks made from this section and from an unfiltered section (not shown). The line shows the PPS phase identified on the SV component section (Figure 3.11).

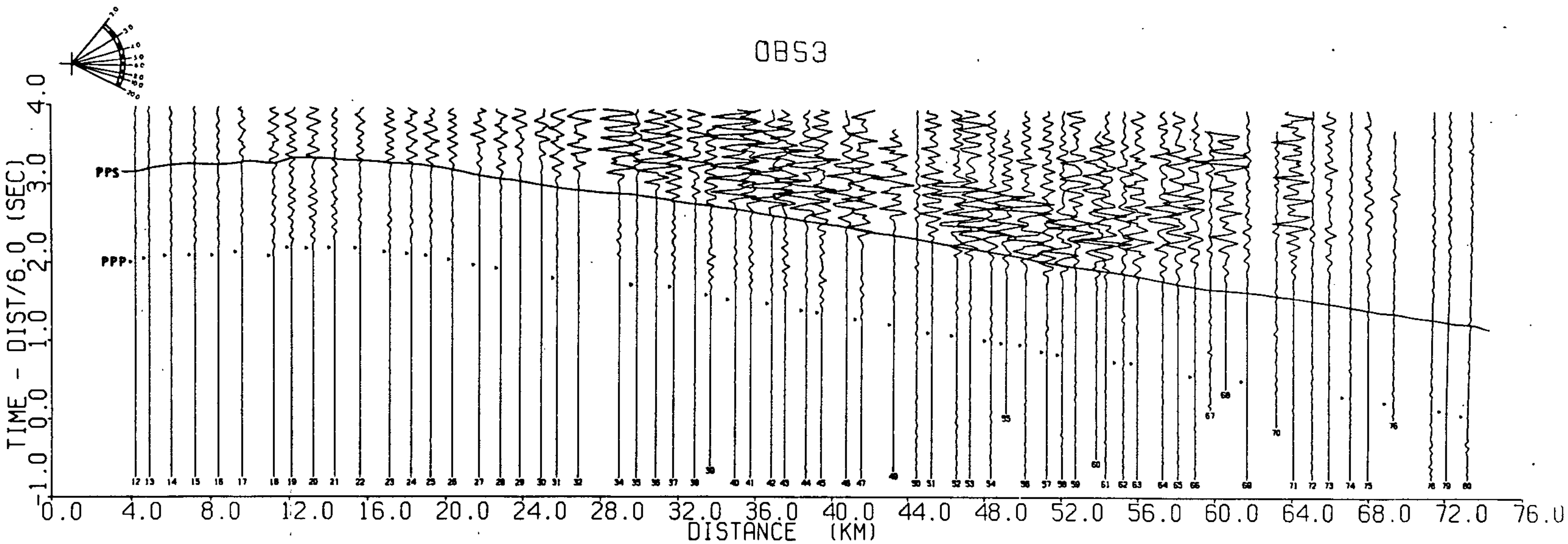

Figure 3.8 Vertical component bandpass filtered (5-20 hz) record section of OBS3. Amplitude corrections, outlined in section 2.5, have been applied. Solid triangles show first arrival picks made from this section to a distance of 40 km. Beyond 40 km, first arrivals are determined from the constant observed time interval between the PPP and the PPS phases as shown in Figure 3.12.

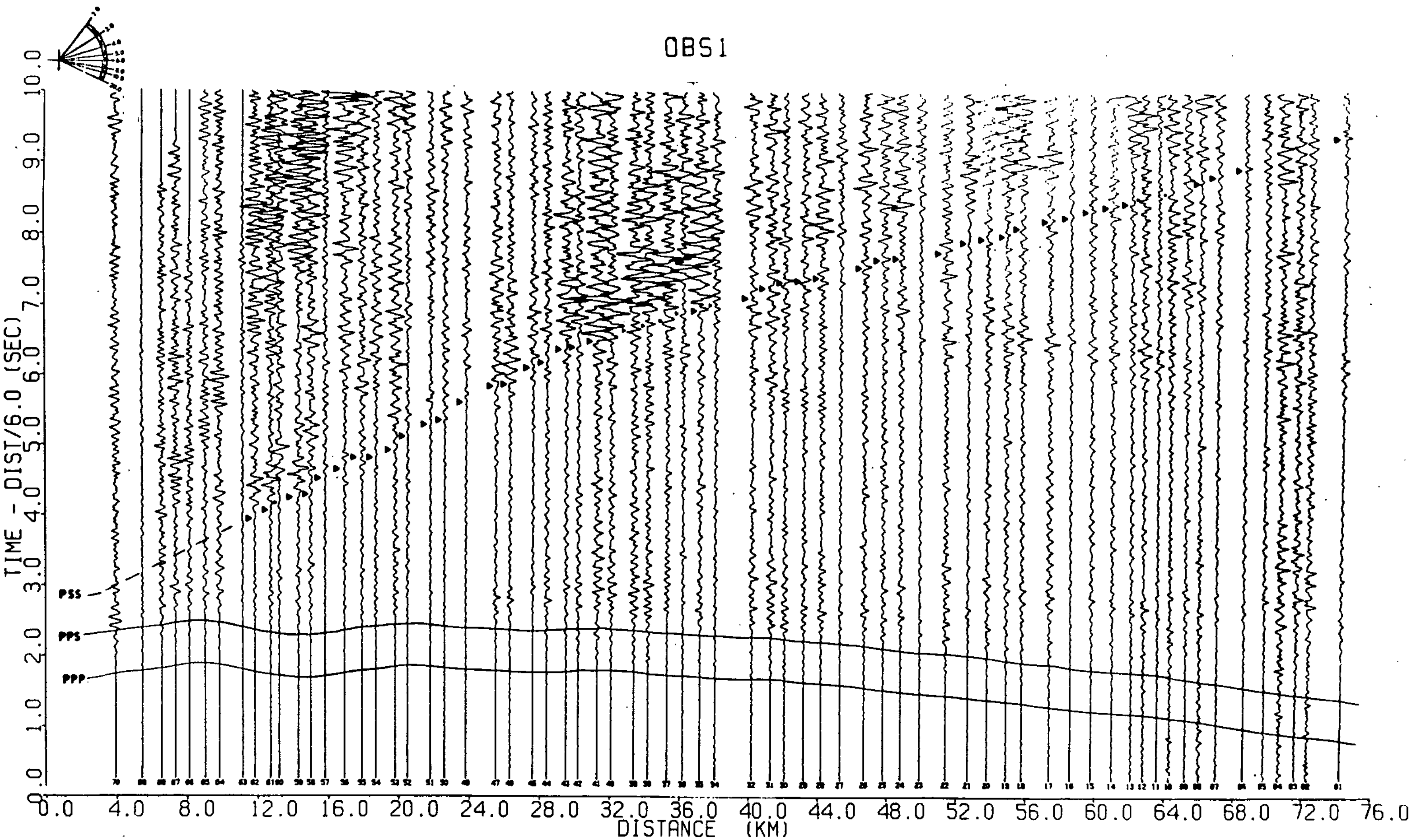

Figure 3.9 Rotated SV component bandpass filtered (5-20 hz) record section of OBS1. All traces have been amplitude corrected. The PPP phase shown in Figure 3.5 has been superimposed. PSS phase is shown by the triangles and timed from this section and that of Figure 3.4.

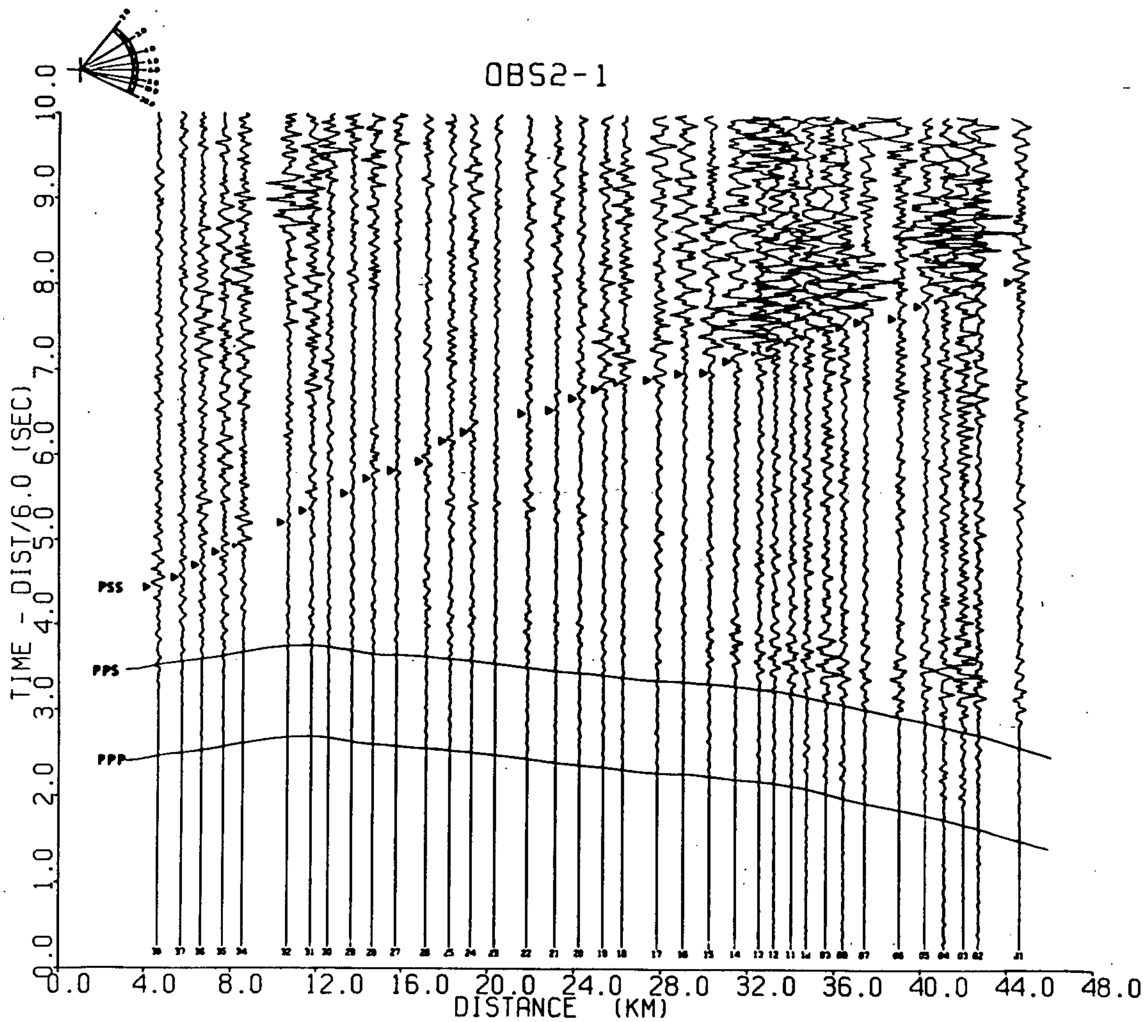

Figure 3.10 Rotated SV-component bandpass filtered (5-20 hz) record section of OBS2 leg 1. All traces have been amplitude corrected. The PPP phase shown in Figure 3.6 has been superimposed. PPS and PSS phases are identified from this section.

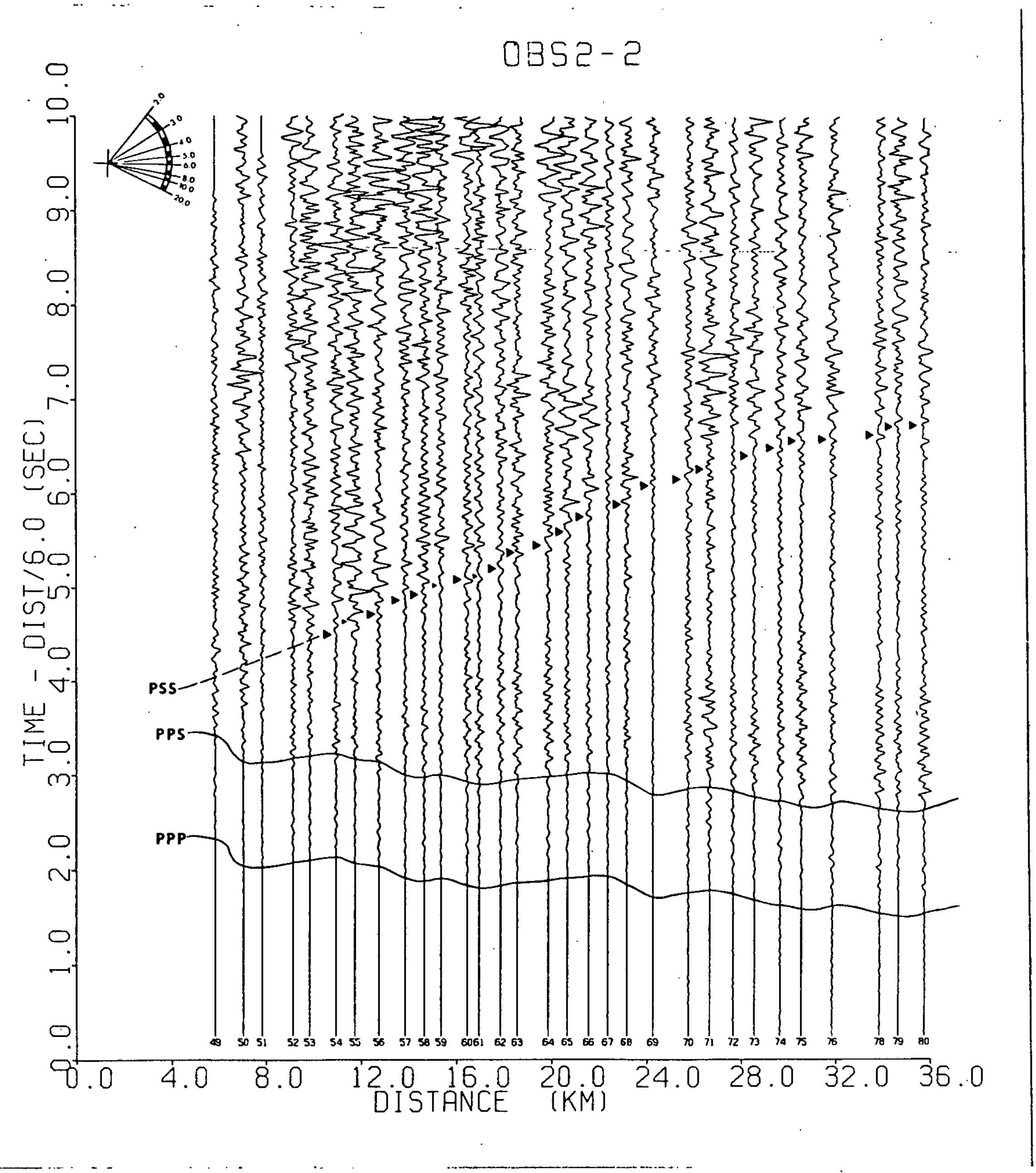

Figure 3.11 Rotated SV component bandpass filtered (5-20 hz) record section of OBS2 leg 2. All traces have been amplitude corrected. The PPP phase shown in Figure 3.6 has been superimposed. PPS and PSS phases are identified from this section.

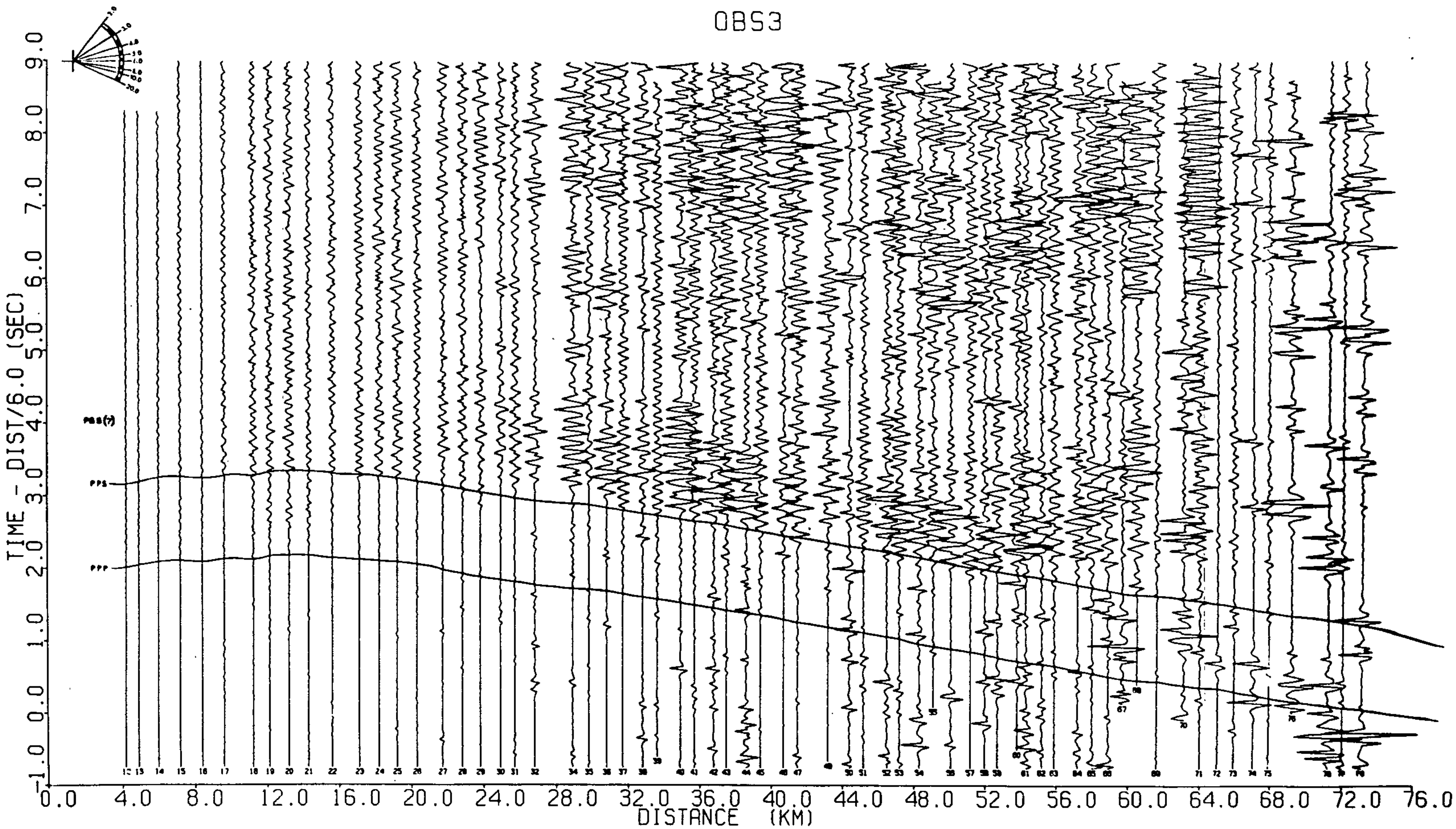

Figure 3.12 Rotated SV component bandpass filtered (5-20 hz) record section of OBS3. All traces have been amplitude corrected. The PPP phase shown in Figure 3.8 has been superimposed. The PSS phase could not be identified.

OBS1 and OBS2 leg 2 are believed to be caused by near-surface lateral velocity inhomogeneities or structural changes. Such a suggestion is consistent with the uppermost crustal structure shown in the pulser profile of Figure 2.3. There are some indications of the same trends for the PSS phase but the identification of the onset is so difficult that minor perturbations are smoothed over.

Besides the three identified phases, no clear secondary refracted or reflected arrivals could be seen on any of the record sections. This is important in terms of the interpreted velocity-depth curves. Except for OBS3, significant increases in amplitude in particular distance ranges are observed for both the PPP and the PSS phases. From the record sections, these are in the range of 30 to 35 km for OBS1, 34 to 42 km for OBS2 leg 1 and 26 to at least 36 km for OBS2 leg 2, respectively. However, the amplitude increase of OBS2 leg 2 is less pronounced than on the other two sections. Apart from the distance ranges just mentioned, amplitude variations with distance are relatively smooth and simple, except for OBS3 in which the reverberation is particularly severe and quite unpredictable. The sudden fade-out of amplitude beyond 55 km, and at travel times greater than the PPS line, is not visible on the reverse line of OBS1 or the partly reversed profile of OBS2 leg 1. No apparent reason could be found except it may due to the instability of instrumental response, as the hydrophone was found to operate intermittently. Therefore, no amplitude analysis has been done for the data from OBS3.

4. TRAVEL TIME INVERSION AND SYNTHETIC SEISMOGRAMS

4.1 Tau inversion :

The tau method (Bessonova et al.,1974), a powerful travel time inversion technique, is particularly applicable to marine seismic data. Often, the assumption of a laterally homogeneous velocity distribution, which is also a piecewise continuous function of depth with a physical lower bound velocity within a low velocity zone, is well satisfied. Therefore, this inversion method has been incorporated by several scientists (Kennett and Orcutt,1976; Orcutt,1976; Kennett et al., 1977) into a standard processing procedure for interpretation of marine refraction profiles.

The tau method is based on the theoretical results of Gerver and Markushevich (1966), in which the travel time data are interrelated with a velocity depth curve V(y) through a function $\tau(p)$,

$$T(p) - pX(p) = \tau(p) = 2\int_0^{Y(p)} [u^2(y) - p^2]^{1/2}\, dy \qquad (4.1\text{-}1)$$

where T and X are the travel time and distance from source to receiver, p is the ray parameter, u is the wave slowness $V^{-1}(y)$, and Y is the depth at which the ray with parameter p turns. In equation 4.1-1, Y(p) can be expressed (Gerver and Markushevich,1966) as

$$Y(p) = \phi(p) + \psi(p) \qquad (4.1\text{-}2)$$

such that

$$\phi(p) = \frac{1}{\pi} \int_p^1 \frac{X(q)}{[q^2 - p^2]^{1/2}}\, dq$$

and

$$\psi(p) = \sum_i \frac{1}{\pi} \int_{y_i}^{\bar{y}_i} \arctan \sqrt{\frac{u^2(y) - q_i^2}{q_i^2 - p^2}}\, dy$$

The function $\phi(p)$ is the usual Herglotz-Wiechert integral. The addition of the term $\psi(p)$ is a generalization which includes low velocity zones; $\bar{y}_i$ and y_i are the depths to the top and bottom of the i-th low velocity zone respectively. q_i (>p) is the ray parameter for the i-th low velocity zone which produces a shadow in the travel time data.

However, it can be shown (Bessonova et al.,1976) that equation 4.1-1 is just Abel's equation. By a modification of equation 4.1-2, the the corresponding inverse formula can be determined to obtain

$$Y(p) = \frac{1}{\pi} \int_0^{\tau(p)} \frac{1}{[v^2(\tau) - p^2]^{1/2}}\, d\tau \qquad (4.1\text{-}3)$$

such that $\tau(p)$ and $v(\tau)$ are mutually inverse functions of each other. Using equation 4.1-3, the extremal bounds for the velocity function can be constructed using the technique introduced by Bessonova et al. (1974,1976). A brief description follows.

Recognition of the function $\tau(p)$ as a singular solution of Clairaut's equation, with the travel time curve T(X) as a free term, is important for the stable estimation of $\tau(p)$ from a discrete number of points on the observed travel time curve. From equation 4.1-1, τ versus X curves for a specified range of p values can be constructed (since T(p) is known). The above-mentioned mathematical property implies that $\tau(X,p)$ has a single stationary point $\tau(p_o)$ for every constant ray parameter p_o. Thus, by finding all the extremal points of the function $\tau(X,p)$ over an interval of p, the travel time data are mapped onto the τ-p plane. The advantage of working in the τ-p domain rather than the p-X plane (McMechan and Wiggins,1972) is that τ is a single-valued, monotonically decreasing function of p, while p may be a multi-valued function of X. Also, derivation of τ in this way is not sensitive to errors in p since a first order error in p only propagates a second order error in τ (Johnson and Gilbert,1972) and this is important for the construction of the function $\tau(p)$ from a given set of travel time data. This makes the error in $\tau(p)$ of the same order as the error in T(X), so that the two extremal bounds of $\tau(p)$ can be determined. As well, the bounds of the inverse function $\nu(\tau)$ are calculated from the bounds of $\tau(p)$. Estimation of the extremal bounds of the velocity-depth function V(y) is obtained from the integration of equation 4.1-3 and conversion from Y(p) to V(y). Finally the extremal bounds are interpolated with a cubic spline. These bounds, however, only limit all possible velocity structures that fit the observed travel time data within its error tolerance. Thus, any velocity-depth curve that lies within the extremal bounds does not necessarily represent a true profile in the region of investigation.

The above formulation is completely general and the presence of one or more low velocity zones is allowed. A low velocity zone in the velocity-depth curve is represented by a sharp jump of τ at constant p in the τ-p plane, just as there is a sharp discontinuity of X at a constant p in the X(p) domain.

The time-distance relations shown in Figures 3.5 to 3.12 are mapped onto individual τ-p planes as described above. The alternate spline smoothing technique (Kennett,1976) or the 'polynomial fit' method (Bates and Kanasewich,1976) are not used, since for the data of this study, the mapping to the τ(p) plane is numerically stable. No distinct jump of τ values is observed in any of the data; consequently, no low velocity zone is inferred. The extremal bounds of the function τ(p) are then inverted to give the corresponding bounds in the function Y(p) and then V(y).

Figure 4.1 shows the extremal bounds of the velocity-depth profiles for both P- and S-wave data recorded on the OBS's. Since the seismic refraction experiment was not designed to sample the surficial sedimentary structure (layer 1 and possibly layer 2), the bounds in Figure 4.1 for the uppermost kilometer are not based on the data set. They are an extrapolation from velocity bounds at a lower depth to the water velocity at the ocean bottom. The extrapolation is essential to the inversion scheme so as to preserve the total travel time behaviour from source to receiver. Analysis of the reflection and shallow refraction data recorded over the same array of OBS's using an airgun source (see section 2.2) should provide more information on the structure of the uppermost crust. However, such a study is outside the scope of this thesis.

4.2 Linearized inversion :

The linearized inversion method of interpreting travel time data (Johnson and Gilbert,1972) also is very applicable to marine seismic data because the assumption of a laterally homogeneous velocity distribution is often well satisfied. However, this technique has suffered from the criticism that it requires a good starting model. With the complementary tau inversion method, there is no difficulty in picking such a model. In fact, Kennett (1976) has shown that the final model is only weakly dependent on all initial models that are within the extremal bounds. Thus, the mean of the extremal bounds is chosen as a starting model for the linearized inversion.

Following Johnson and Gilbert (1972), the function $\tau(p)$ is used as the datum for the linearized inversion scheme. To first order of approximation, $\delta\tau(p)$ can be treated as a linear functional of $\delta u(y)$ (Julian and Anderson,1968) in equation

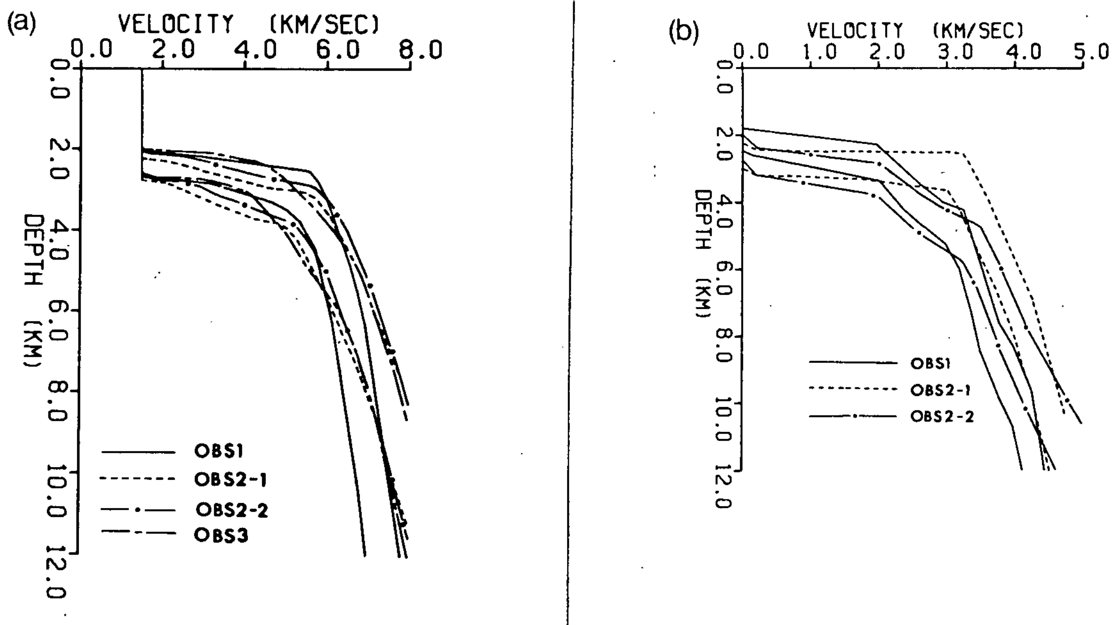

Figure 4.1 Extremal bounds of velocity-depth profiles for travel time data in Figures 3.5 to 3.12.

(a) P-wave.

(b) S-wave.

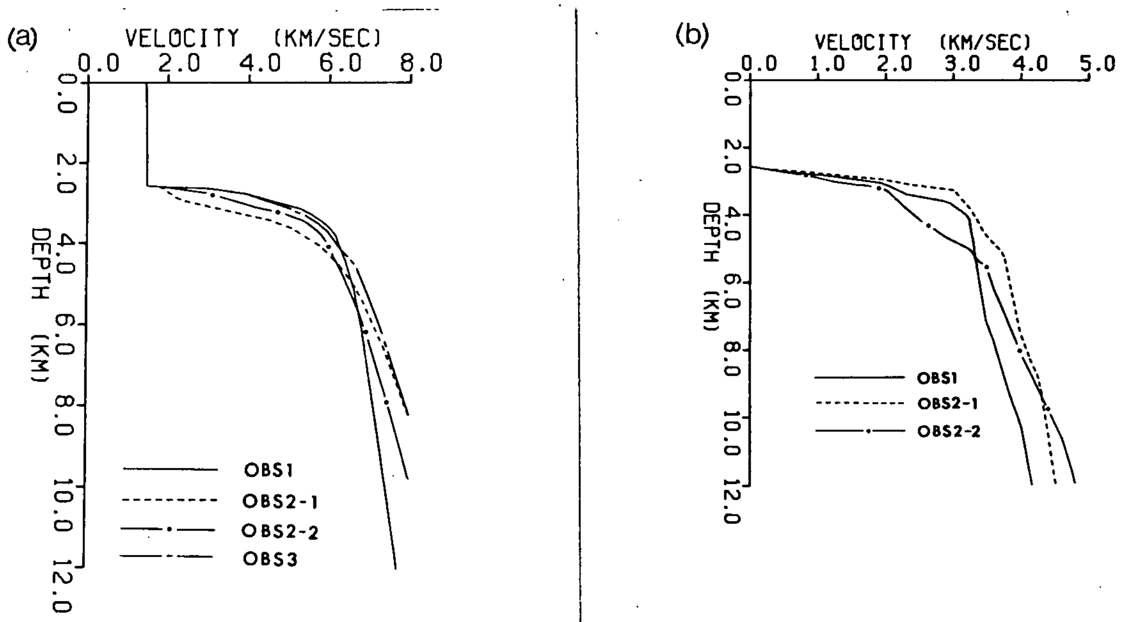

Figure 4.2 Velocity-depth profiles from linearized inversion of the travel time data shown in Figures 3.5 to 3.12.

(a) P-wave.

(b) S-wave.

4.1-1 such that

$$\delta\tau(p) = 2\int_0^{Y(p)} \frac{u(y)\,\delta u(y)}{[u^2(y) - p^2]^{1/2}}\,dy \tag{4.2-1}$$

Thus, $\delta\tau$ can be expressed as a combination of kernels $G_i(y)$ and velocity functions so that

$$\delta\tau_i = \int_0^{Y_m(p)} G_i(y)\,m(y)\,dy \tag{4.2-2}$$

in which

$$m(y) = \frac{\delta u(y)}{u(y)} = -\frac{\delta V(y)}{V(y)}$$

and

$$G_i(y) = \frac{2u^2(y)}{[u^2(y) - p^2]^{1/2}} \quad , \quad 0 \le y \le Y_m(p)$$

$$= \quad 0 \quad , \quad y \ge Y_m(p)$$

In equation 4.2-2, $Y_m(p)$ is the maximum depth to be considered in any velocity model.

Using the technique described in section 4.1, a set of N values $\tau_i(p_i)$ with variances θ_i^2 can be constructed from the observed travel time data. Further, if γ_i are the differences between the observed $\tau_i(p_i)$ for the real earth and the $\tilde{\tau}_i(p_i)$ calculated from a particular trial model, and if γ_i are small with respect to T_i, then δT_i in equation 4.2-2 can be replaced by γ_i in the hope that a minor perturbation of m(y) could bring the trial model into agreement with the observations. Therefore, the condition (Johnson and Gilbert, 1972)

$$\gamma_i - \theta_i \leq \int_0^{Y_m(p)} G_i(y)m(y)\,dy \leq \gamma_i + \theta_i , \qquad (4.2\text{-}3)$$

$$i = 1,\ldots,N$$

is required. In order to satisfy equation 4.2-3 in a least square sense and simultaneously avoid the singularity in $G_i(y)$, equation 4.2-3 is first integrated by parts. Thus

$$\gamma_i - \theta_i \leq \int_0^{Y_m(p)} J_i(y)m'(y)\,dy + J_i(0)m(0) \leq \gamma_i + \theta_i , \qquad (4.2\text{-}4)$$

$$i = 1,\ldots,N$$

such that

$$J_i(y) = \int_y^{Y_m(p)} G_i(s)\,ds$$

is a set of new kernels and the prime denotes differentiation with respect to y. $J_i(y)$ can be interpreted physically as the travel time from the level y to the depth at which the ray with parameter p turns. A discontinuity in the velocity-depth curve at a depth y=c could be accounted for by the introduction of an additional term $J_i(c)[m(c+)-m(c-)]$. Thus, J_i could be calculated easily for any trial model. Then, using the 'flattest' perturbation criteria of Backus and

Gilbert (1969), i.e. the search for the minimum of the function

$$\frac{1}{2}\int_0^{Y_m(p)} [m'(y)]^2\,dy \quad + \quad \frac{1}{2}\,m^2(0) \qquad (4.2\text{-}5)$$

subject to the constraints of equation 4.2-4, a final model is achieved after successive iterations. This final model, which has the tendency to minimize velocity gradients is more realistic than the conventional layered model. Also, the final model is more consistent with frequently observed results from recent seismic refraction studies than is the layered model; namely the presence of prominent first arrivals and the general absence of distinct secondary arrivals, except in some instances for wide-angle reflections from the M-discontinuity (Orcutt et al.,1976; Whitmarsh,1978).

Velocity-depth curves derived from the application of this linear inversion method to the travel time data for both P and S waves are shown in Figure 4.2. Again for the reason given in section 4.1, all velocity-depth structures in the uppermost kilometer are not derived from the data set. The curves shown represent extrapolation from velocities at a lower depth to the water velocity at the ocean bottom.

4.3 Synthetic seismograms :

The two inversion procedures discussed above are based on travel time data only. Interpretation using synthetic seismograms makes use of the additional information contained in the data, namely amplitude changes along the profile. Such information puts additional constraints on acceptable velocity-depth models. No joint inversion technique using both travel times and amplitudes has been published, but theoretical work in this direction is being pursued by some researchers.

In this study, synthetic seismograms are calculated by the disk ray theory (DRT) approach described by Wiggins (1976), and for which the theoretical derivation is provided by Chapman (1976a,b). The advantages and disadvantages of DRT calculations have been discussed by Malecek and Clowes (1978) in the first published interpretation of marine seismic data using DRT synthetic seismograms. The most important aspect of the DRT method is that it is computationally efficient and thus inexpensive. Many models can be tried, facilitating the desire to obtain the best fit of computed travel times and amplitudes with the observed seismograms.

The use of the computer algorithm, HRGLTZ, (coded by R.A.Wiggins), in which the DRT computations are made can be related to the basic equation 4.1-1. In this equation, the τ term can also be expressed (Wiggins and Madrid, 1974) as

$$\tau = \int_{p}^{\bar{p}} X(p)\,dp \qquad (4.3\text{-}1)$$

such that the equation can be re-written as

$$T(p, X) = pX + \int_{p}^{\bar{p}} X(p)\,dp \qquad (4.3\text{-}2)$$

where $\bar{p}$ is the maximum p value. Equation 4.3-2 relates the travel time of an arrival to the area under the X(p) curve. Similarly, the amplitude of an arrival can be expressed as a function of p and X through the relation

$$A(p,X) = F(p,X)\left|\frac{dp}{dX}\right|^{1/2} \tag{4.3-3}$$

In equation 4.3-3, F(p,X) is a slowly varying complex function of p and X compared to the second factor, $|dp/dX|^{1/2}$ (Bullen,1965). Thus to a close approximation, equation 4.3-3 relates the amplitude of an arrival to the square root of the slope of the p-X curve. Because of this direct relation of the X(p) curve to travel times and amplitudes, synthetic seismogram calculations using DRT are best done with input in the p-X plane rather than in the velocity-depth domain (Wiggins and Madrid,1974; McMechan,1976).

To obtain initial models, P-wave velocity-depth profiles from the linearized inversion (see Figure 4.2a) are used in the program MDLPLT also written by R.A.Wiggins. This program interpolates the input velocity-depth profiles and generates the corresponding p-X curves. These form the input data for HRGLTZ to compute the DRT theoretical seismograms for comparison with the observed OBS records. Since the input p-X curve has satisfied the travel time relation in a best fit sense, simultaneously changing the slope of the p-X curve and keeping the area under the curve constant will produce synthetic record sections with different amplitude characteristics but identical travel times. This trial-and-error procedure is repeated until an acceptable fit of the synthetic seismograms to the observed data is attained.

Figures 4.3 to 4.5 show the DRT synthetic seismograms for profiles OBS1 and OBS2. The source wavelet which was convolved with the calculated DRT impulse response is given on the upper right. It was derived from a clear first arrival on the OBS2 profile. In Figure 4.6, the velocity-depth profiles corresponding to the synthetic sections are displayed. Synthetic seismogram matching was not done for OBS3 (AGC instrument) since the amplitude information was considered unreliable, as discussed in section 3.5. Also, no attempt was made toward the modelling of the PSS phase at all since no suitable computer algorithm could be implemented.

Figures 4.3 to 4.5 compare well with the observed data (PPP phase) shown in Figures 3.5, 3.6 and 3.7. Note particularly that the irregular trend of arrivals probably caused by surface velocity inhomogeneities cannot be modelled by DRT. As well, because the starting model is chosen from the linearized inversion interpretation, preference is given to velocity-depth models that possess the least changes in velocity gradient rather than step-like increases in velocity (see the sketch below).

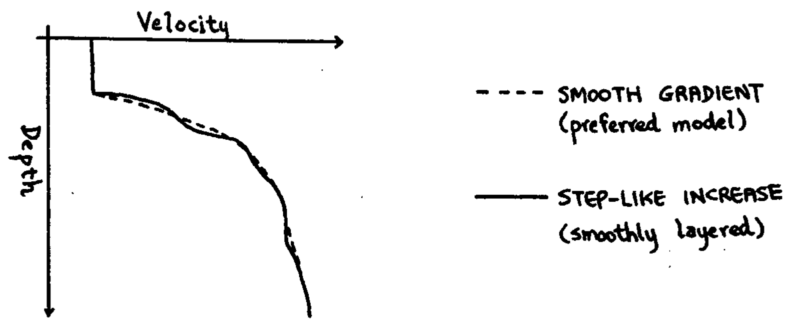

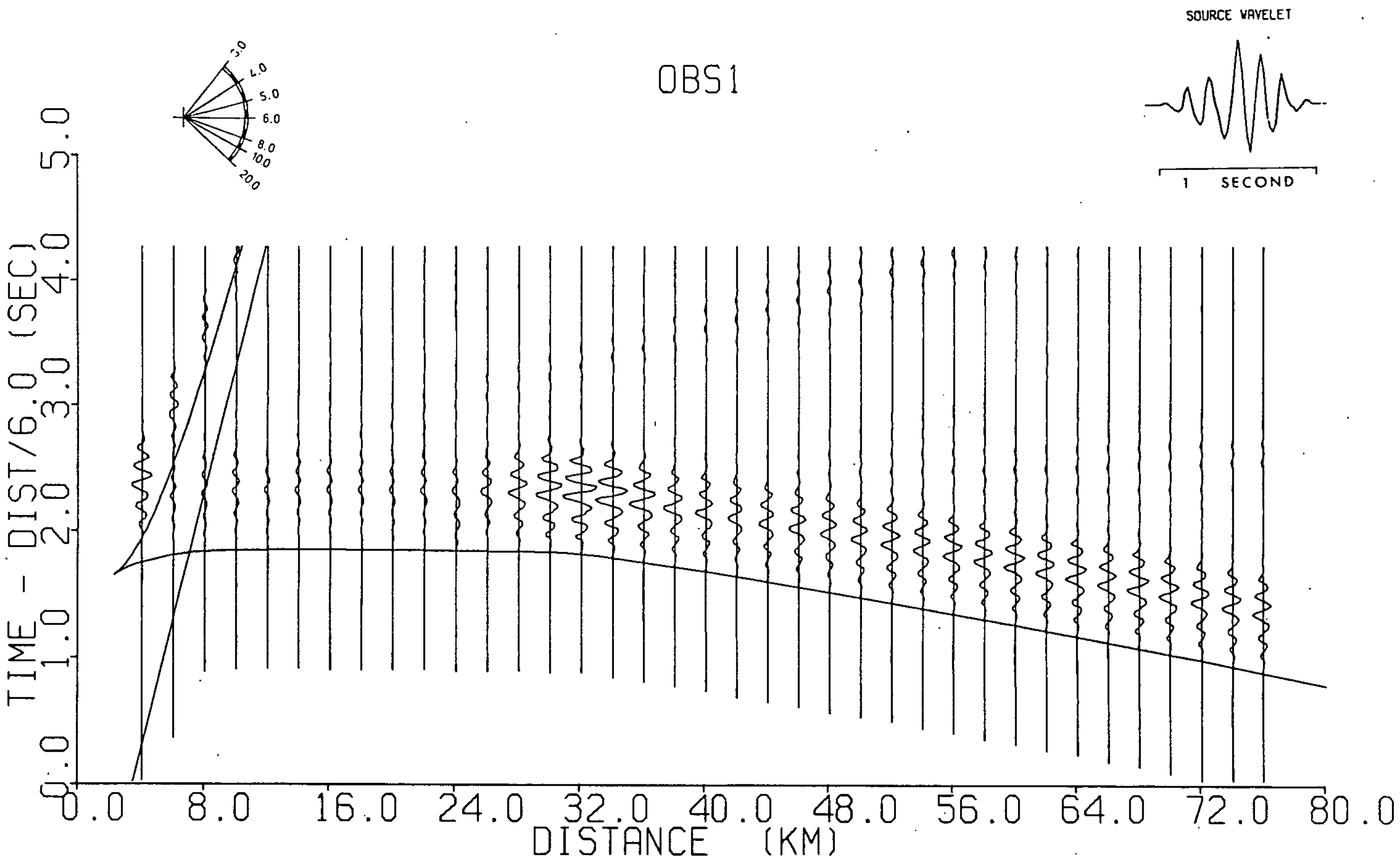

Figure 4.3 Computed DRT synthetic seismograms and travel times for data of OBS1. The source wavelet convolved with the impulse response from the synthetic calculation is also shown. Compare with Figure 3.5.

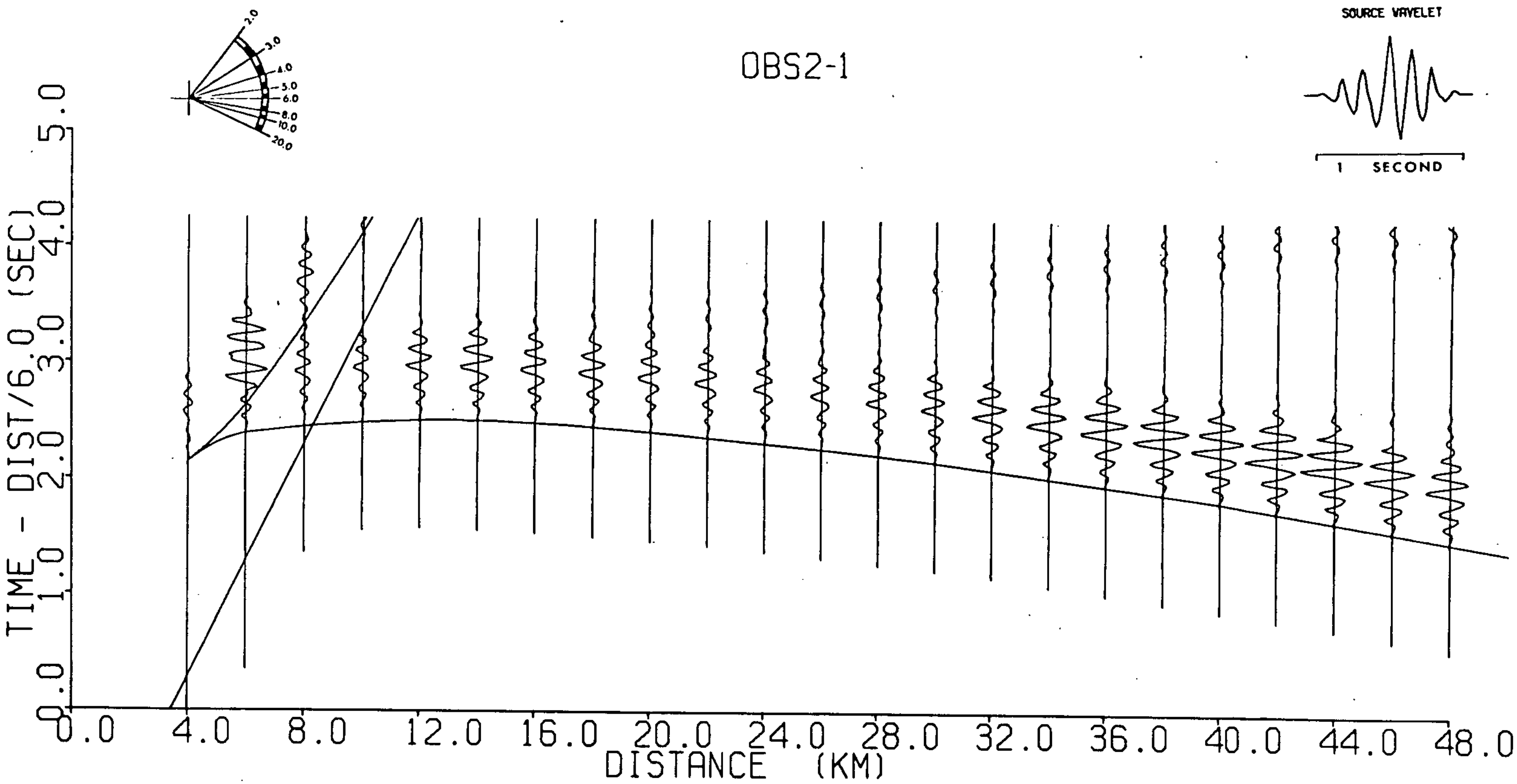

Figure 4.4 Computed DRT synthetic seismograms and travel times for data of OBS2 leg 1. The source wavelet convolved with the impulse response from the synthetic calculation is also shown. Compare with Figure 3.6.

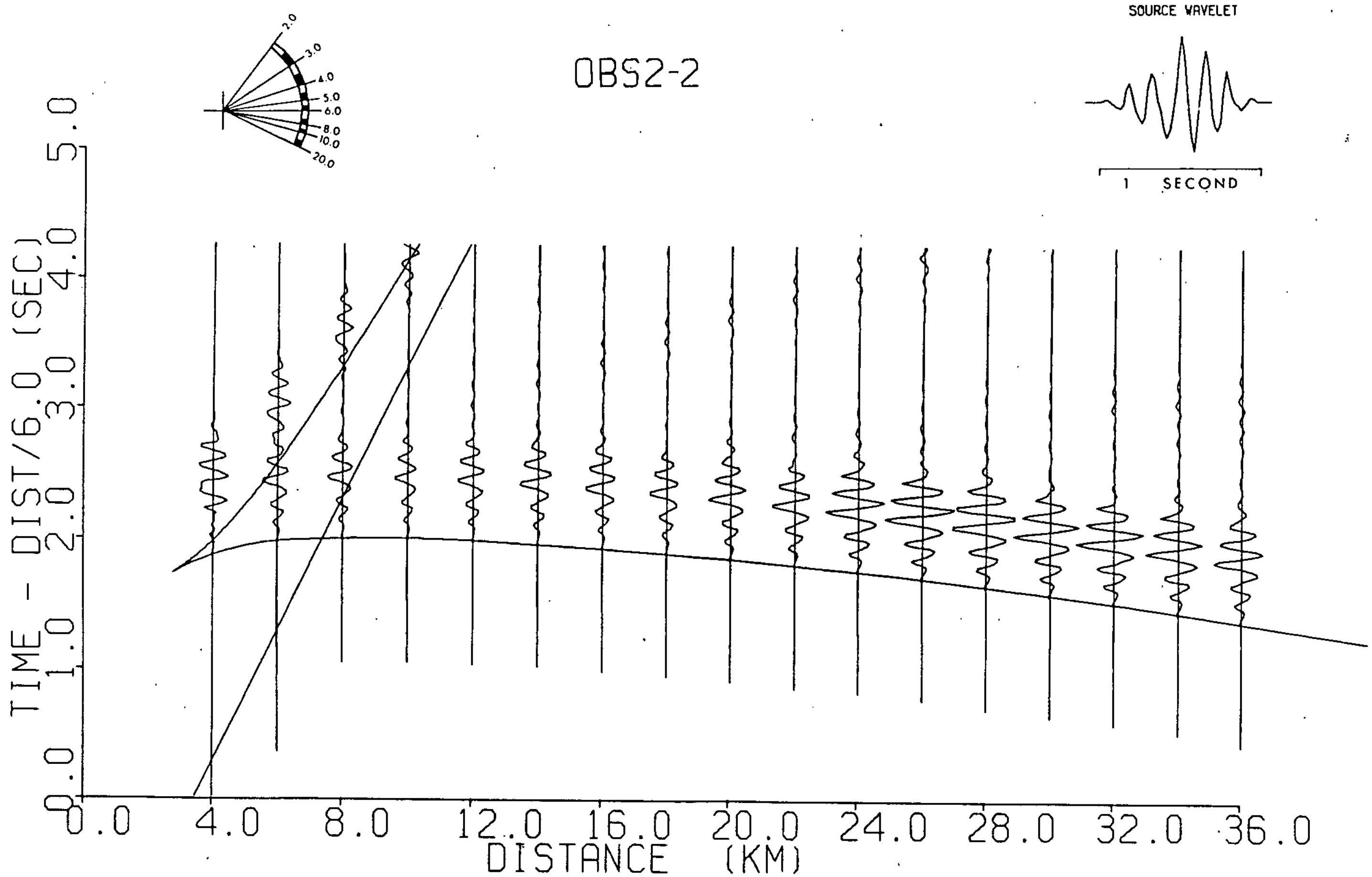

Figure 4.5 Computed DRT synthetic seismograms and travel times for data of OBS2 leg 2. The source wavelet convolved with the impulse response from the synthetic calculation is also shown.

Compare with Figure 3.7.

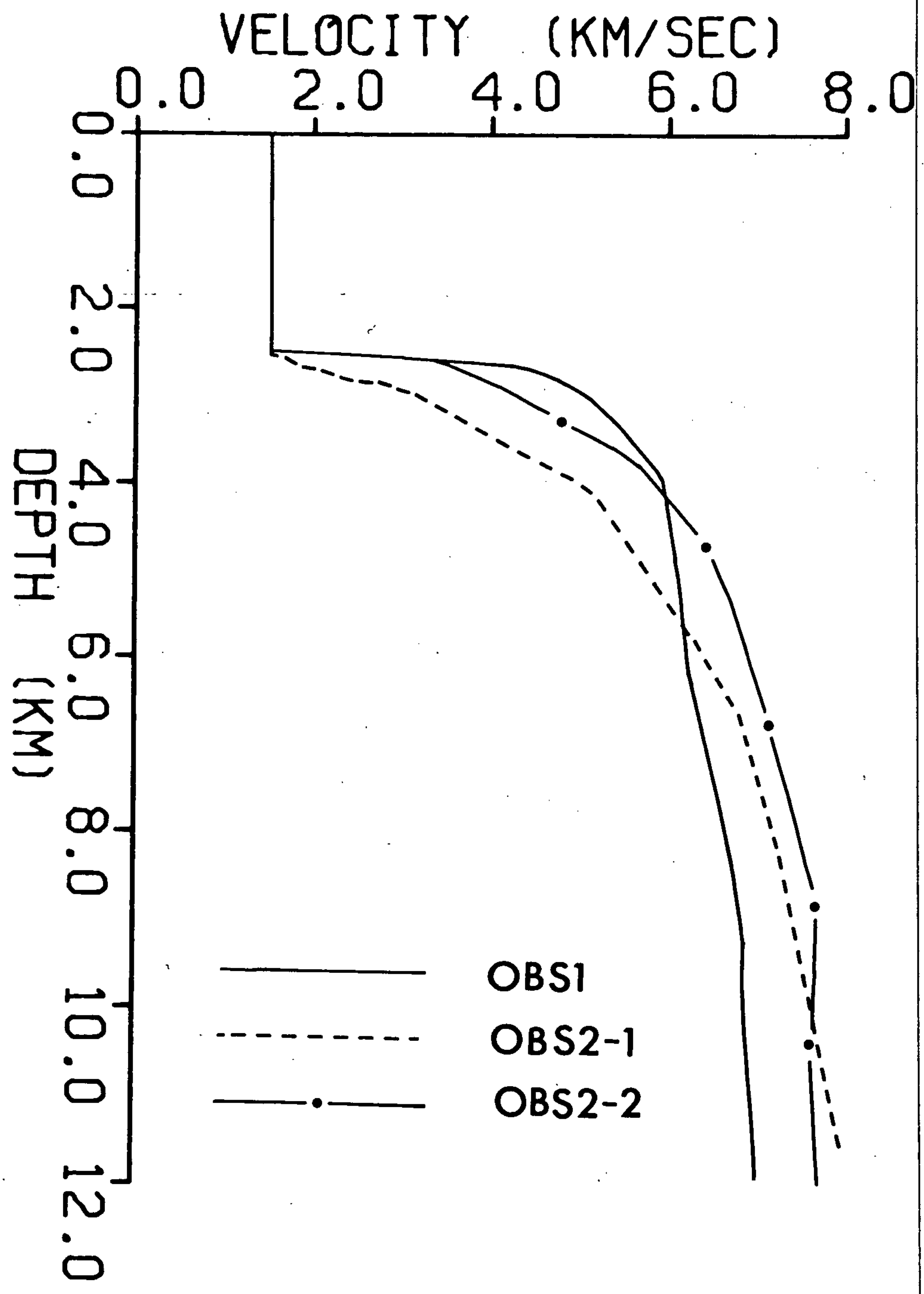

Figure 4.6 P-wave velocity-depth curves obtained from the DRT synthetic seismogram calculations shown in Figures 4.3 to 4.5.

The preferred model does not produce prominent secondary arrivals, consistent with the observed data. But, depending on the gradient between 'layers', the smoothly layered model may produce such phases. However, in testing this point, it has been possible to generate a set of synthetic seismograms, similar to those shown in Figures 4.3 to 4.5, from smoothly layered models with small velocity gradients. Thus, fine structural details of velocity-depth profiles cannot be resolved with the existing data set. The P-wave velocity-depth profiles shown in Figure 4.6 represent the most likely models consistent with both travel times and amplitudes of the observed seismograms.

5. DISCUSSION

Velocity-depth curves (Figures 4.1 and 4.2) derived from the travel time inversion techniques discussed in sections 4.1 and 4.2 are based on refracted first arrival times (PPP and PSS phases) only. Thus, details of any structural transitions are concealed and cannot be resolved (Kennett and Orcutt, 1976; Kennett et al., 1977). With the aid of DRT synthetic seismogram modelling procedures, the P-wave velocity-depth models from linearized inversion are further refined (Figure 4.6) to satisfy both travel time and amplitude characteristics. Since no amplitude analysis has been done to refine the S-wave velocity-depth curves after linearized inversion, those displayed in Figure 4.2b are considered final, though by no means unique. Unless otherwise stated, these S-wave velocity-depth profiles together with the DRT P-wave velocity-depth models (Figure 4.6) are used for interpretation purposes.

Both the P- and S-wave models display a very high velocity gradient in the uppermost 0.5 km of the crust with a sharp decrease at a depth of 1 to 2 km below the ocean floor. As discussed before, the data do not define well the velocity structure in the uppermost kilometer, but to reach the velocity values at greater depths, a substantial gradient must exist. Recall from section 2.4 that an average sediment thickness of 324 km (0.18 sec 1-way time at a velocity of 1.8 km sec^{-1}) is assumed. In terms of conventional interpretations which subdivide the oceanic crust into layers (e.g. Houtz,1976; Whitmarsh,1978), the change in velocity gradient is correlated with the transition from layer 2 to layer 3. The transition is believed to represent a compositional change from metabasalt or diabase to gabbro (Peterson et al.,1974) or a structural change from brecciated dikes to sheeted dikes (Salisbury and Christensen,1978).

The boundary between layer 3 and the upper mantle (the M-discontinuity) is not clearly defined on the velocity-depth curves for either P or S waves. But a close examination of Figures 4.2b and 4.6 shows that a slight change in gradient occurs at depths between 8.8 and 10 km. In particular, the P-wave model, which is better constrained, shows a visible gradient change at depths of 9.2 km for OBS1 and 8.8 km for OBS2 leg 2 although OBS2 leg 1 reveals no comparable change. These changes in gradient are interpreted as representing the transition from crust to mantle, giving a sub-bottom crustal thickness in the range of 6.5 km. On the basis of this interpretation, upper mantle apparent velocities lie in the range from 6.9 to 7.8 km sec^{-1} for P waves and 3.9 to 4.6 km sec^{-1} for S waves where the lower values are from OBS1 and the higher ones from OBS2 leg 2.

This asymmetry in upper mantle velocities could be seen in all velocity-depth profiles (Figure 4.1, 4.2 and 4.6) derived in chapter 4. In fact, the asymmetries exist not only between OBS1 and OBS2 leg 2 but between OBS1 and all the other OBS's at depths greater than 6 km. As the analyses are based on a laterally homogeneous model, the asymmetry in velocities suggests that the crust-mantle interface dips away from the ridge. By assuming reversed upper mantle apparent P-wave velocities of 6.9 and 7.8 km sec^{-1} and a dipping M-discontinuity underlying an assumed homogeneous crustal layer of 6 km sec^{-1}, a P-wave velocity of 7.3 km sec^{-1} for the upper mantle is determined. The calculated dip is approximately 10° away from the ridge. Changing the assumed velocity of the overlying crust does not alter the end result significantly. A similar calculation using S-wave values yields an upper mantle velocity of 4.2 km sec^{-1}, assuming an average S-wave crustal velocity of 3.3 km sec^{-1} corresponding to a Poisson's ratio of 0.29 (Christensen and Salisbury,1975). Since the partly reversed profile between OBS3 and OBS2 leg 1 displays only a small asymmetry in velocities (Figure 4.1a and 4.2a), the dipping crust-mantle interface probably is confined principally to the region (35 km in length) between OBS2 and the ridge axis. This suggests that the M-discontinuity dips more steeply near Explorer ridge than it does farther from it.

The foregoing interpretation of crustal thickness (~6.5 km) and upper mantle P-wave velocity (7.3 km sec^{-1}) lies within the range reported for other studies near axial zones (Le Pichon et al.,1965; Keen and Tramontini,1970; Talwani et al.,1971; Poehls,1974). In contrast, a recent seismic refraction study over Juan de Fuca ridge (Davis et al.,1976) suggested an abnormal crustal thickness of 10 to 11 km. The crustal thickness as interpreted was due to a localized low velocity mantle near the spreading ridge and directly under the OBS's. This caused a time residual to be observed even though the travel time branch corresponding to mantle arrivals would be correctly representative of the apparent velocity along the ridge flank. As a result, the delay in intercept time would be interpreted erroneously as a deep interface. They also recommended that the above explanation could be checked easily by reversing the cross profile or simply by doing another refraction line on the flank. Malecek and Clowes (1978) have done both in a seismic refraction experiment over the southern Explorer ridge and on Explorer plate. However, their results still required an anomalously thick crust of 8 to 10 km. As well, Pn velocities ranging from 7.8 km sec^{-1} perpendicular to the ridge to 7.3 km sec^{-1} parallel to it were interpreted from the reversed profiles. These authors suggest that the abnormal crustal thickness may be the general tectonic result of two small plates jammed between two large plates. In particular, they postulate that the cause may be due to the 'bunching-up' effect of the young crust (<3.5 m.y.) of Explorer plate on 'collision' with the giant North America plate. Whether the proposed hypothesis is correct or not is a subject of conjecture and future research. However, the common occurrence of an anomalously thick crust in Explorer plate and possibly Juan de Fuca plate is required to satisfy all existing seismic refraction studies, the two mentioned above plus those of Lynch (1977) and Thorleifson (1978) in Winona basin.

No further attempt is made here to explain the existence of an anomalously thick crust (8-10 km) in Explorer plate. But the normal crustal thickness (~6.5 km) and anomalously low P-wave upper mantle velocity (7.3 km sec^{-1}) derived from this study on the Pacific plate contrast markedly with the equivalent values on Explorer plate. This leads one to question whether the M-discontinuity has been interpreted correctly in this study. If the crust-mantle interface actually occurs at a greater depth than 6.5 km and has a relatively rapid transition to a normal northeastern Pacific upper mantle velocity of 8.1 km sec^{-1} (Keen and Barrett,1971), a prominent post-critically reflected phase should appear as a secondary arrival in the compiled record sections. No such phase is visible so the interpretation as discussed is the one most consistent with the data. Therefore, the small change in velocity gradient between 6.2 to 7.4 km below the ocean bottom may be a realistic representation for a gradual transition from lower crust to upper mantle. Also, it is worthwhile to point out that all P-wave velocity-depth models except OBS1 are within the extremal bounds derived from seismic refraction studies near the East Pacific Rise for crust of less than 5 m.y. old (Kennett et al.,1977).

Besides the usual interpretation in terms of the velocity-depth profiles, a further attempt was made to estimate Poisson's ratio (σ) in the region of study. Such estimates are based on the standard relation (Bullen,1965)

$$\sigma = \frac{(V_P/V_S)^2 - 2}{2(V_P/V_S)^2 - 2} \qquad (5.1\text{-}1)$$

where V_P and V_S are the P- and S-wave velocities. Figure 5.1 shows the calculated Poisson's ratio values as a function of depth. The four different curves marked LO, HI, LN and DL represent differences in the basic data from which they are calculated. LO and HI symbolize Poisson's ratios derived from the two extremal bounds (lower and upper) of velocities (see Figure 4.1); LN stands for Poisson's ratios calculated from results of linearized inversion (see Figure 4.2); DL refers to Poisson's ratios computed from the P-wave velocity-depth structure derived from DRT synthetic seismograms (see Figure 4.6) and S-wave velocity-depth structure from linearized inversion (see Figure 4.2b). Since the velocity-depth structures on which the calculation of Poisson's ratio was based have a low resolving power (see discussion earlier) on structural details, only general discussions are warranted.

For OBS1 and OBS2 leg 1, all four curves scattered widely with the line LN having an upper bound characteristic, whereas for OBS2 leg 2, the curves have a tendency to cluster together. While the reliability of the Poisson's ratio data is poor, they indicate a tendency to be between values of 0.25 and 0.32 in the deeper crust and somewhat greater in the upper crust (although OBS2 leg 1 is an exception). Only the curve DL in OBS1 compares favourably with laboratory data on Poisson's ratio derived from sampled rocks in the Bay of

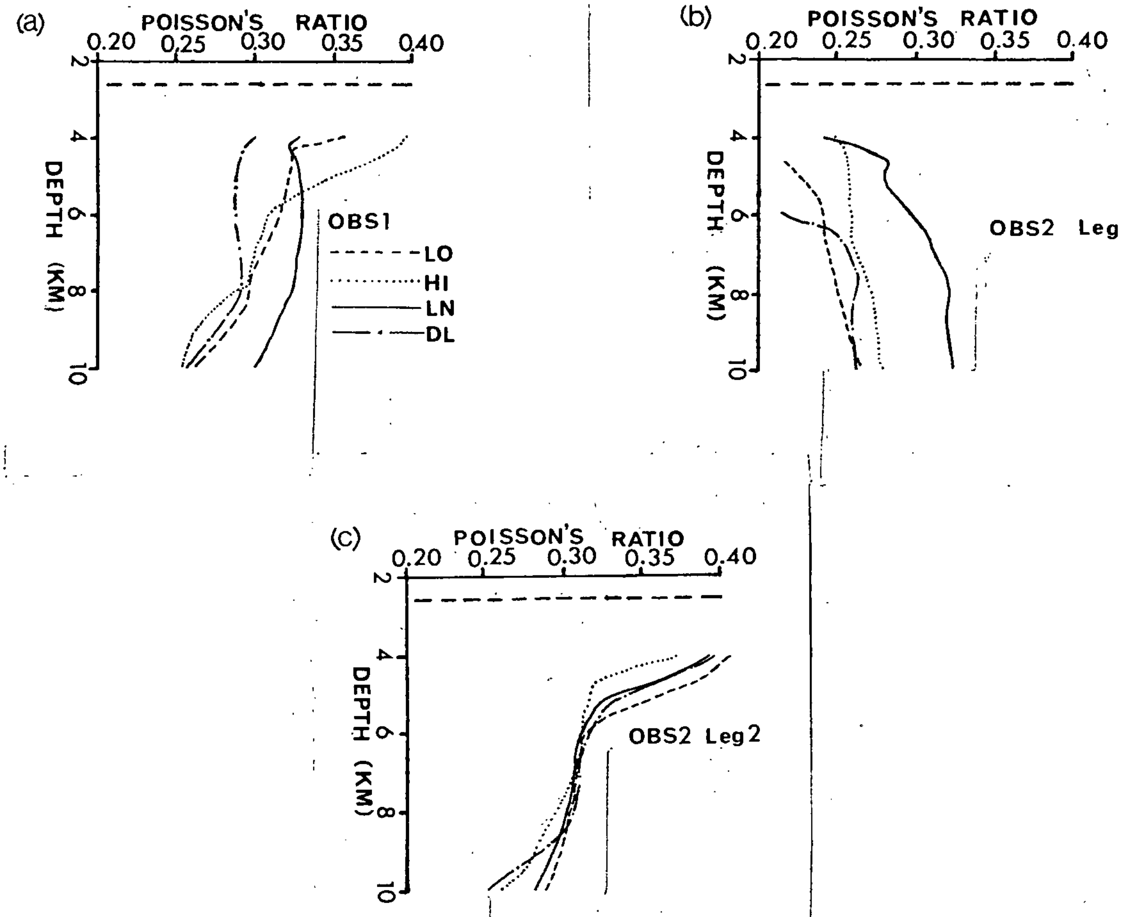

Figure 5.1 Poisson's ratio as a function of depth for (a) OBS1, (b) OBS2 leg 1 and (c) OBS2 leg 2. The four curves represent calculations from different P- and S-wave velocity-depth profiles. LO and HI represent ratios derived from lower and upper extremal bounds of the velocities; LN from velocities determined by linearized inversion; DL from P-wave velocity-depth structures based on DRT synthetics and S-wave velocity-depth profiles from linearized inversion. The dashed line at 2.6 km is the water bottom. For additional discussion, see text.

Islands ophiolite complex in Newfoundland (Salisbury and Christensen,1978). The data set presented here is believed to be a first attempt to derive Poisson's ratio as a function of depth from OBS seismograms. Because of the sensitivity of Poisson's ratio to changes in the ratio of P- and S-wave velocities, much better constrained velocity-depth curves are required before meaningful geological interpretations can be made.

In Figure 5.1, no Poisson's ratio was calculated for the uppermost 1.5 km below sea bottom since the corresponding velocity interval is based on extrapolation from the data set (see section 4.2). However, through the estimation of an average S-wave sediment velocity over each OBS by using the observed constant interval time between the PPP and the PPS phases, and assuming a constant P-wave sediment velocity of 1.8 km sec^{-1} (Talwani et al.,1971; Peterson et al.,1974), an average Poisson's ratio can be derived. Table 5.1 summarizes the results. The sediment thickness is derived from the pulser profile shown in Figure 2.3, as discussed in section 3.1. Using a lower average P-wave sediment velocity would decrease the tabulated Poisson's ratios slightly but not significantly. Noting that σ=0.5 for a liquid, the high values of Poisson's ratio suggest a very poorly consolidated sediment. This interpretation is consistent with conclusions made in comparable studies (Davis et al.,1976; Lewis and McClain,1977). More detailed information on the physical properties of the sediments (thickness and degree of compaction) could prove useful for interpreting heat flow data and understanding the tectonic activity in the area.

Site	Thickness (m)	PPP-PPS (sec)	S-wave velocity (km sec^{-1})	Poisson's ratio
OBS1	99	0.60	0.17	0.495
OBS2	225	1.10	0.20	0.490
OBS3	315	1.15	0.27	0.488

TABLE 5.1

Average S-wave sediment velocities and Poisson's ratios from time differences in PPP and PPS phases.

6. SUMMARY

Through the use of travel time inversion techniques and amplitude analyses, three-component seismograms recorded on an array of three OBS's deployed on the Pacific plate immediately west of Explorer ridge have been interpreted. The refracted S-wave arrivals are identified and timed on most sections by the combined use of the rotated SV component record sections and the polarization filtered data. This enables two travel time inversion techniques, tau and linearized inversions, to be applied on both P- and S-wave travel times. The tau inversion gives extremal velocity-depth bounds such that all models which satisfy the travel time data must lie inside. The linearized inversion seeks a best fit model within the extremal bounds under the constraint of least change in velocity gradient. The use of DRT synthetic seismograms further refine the resultant velocity-depth models to satisfy the observed amplitude characteristics.

All final models, as interpreted, show a pronounced velocity gradient in the upper crust, a somewhat lesser gradient in the lower crust, and a gradual transition to the upper mantle. No velocity discontinuities are required to satisfy the data. A normal oceanic crustal thickness of 6.5 km and a reversed Pn velocity of 7.3 km sec^{-1} are interpreted. The latter is relatively low but is consistent with Pn velocities derived from comparable studies near axial zones where young, immature lithosphere is present.

From the P- and S-wave velocity-depth curves, Poisson's ratios are calculated to be in the range of 0.25 to 0.32, at a sub-bottom depth of 4 to 10 km, with the higher values found in the upper crust. However, resolution of the velocity-depth profiles is not adequate to determine Poisson's ratios such that a meaningful geological interpretation can be made.

In terms of the principal tectonic results for the region west of Explorer ridge on the Pacific plate, the normal oceanic crustal thickness (and low Pn velocity) contrast markedly with the thick crust of Explorer and Juan de Fuca plates, located east of the ridge system (Malecek and Clowes,1978; Davis et al.,1976). Assuming the classical theory of sea-floor spreading at a ridge, the disparate results on either side of Explorer ridge, give support to the suggestion by Malecek and Clowes (1978) that the thick crust is the result of compressive interaction between the young, small Explorer plate and the older, larger North America plate. It is hoped that in the future, more geophysical and geological studies will provide an integrated explanation of the uncertain geodynamical features in this complex tectonic region of the north-eastern Pacific.

REFERENCES

Atwater,T. (1970)
Implications of plate tectonics for the Cenozoic tectonic evolution of western North America. Bull. Geol. Soc. Amer., V81, pp.3513-3536.

Backus,G. & Gilbert,F. (1969)
Construction of P-velocity models to fit restricted sets of travel time data. Bull. Seism. Soc. Am., V59, pp.1407-1414.

Barr,S.M. & Chase,R.L. (1974)
Geology of the northern end of Juan de Fuca Ridge and sea-floor spreading. Can. J. Earth. Sci., V11, pp.1384-1406.

Basham,P.W. (1967)
Time domain studies of short period teleseismic P phases. Unpublished MSc thesis, University of British Columbia. 145pp.

Bates,A.C. & Kanasewich,E.R. (1976)
Inversion of seismic travel times using the tau method. Geophys. J. Roy. astron. Soc., V47, pp.59-72.

Bessonova,E.N., Fishman,V.M., Ryaboyi,V.Z. & Sitnikova,G.A. (1974)
The tau method for inversion of travel times I. Deep seismic sounding data. Geophys. J. Roy. astron. Soc., V36, pp.377-398.

----- Fishman,V.M., Shnirman,M.G., Sitnikova,G.A. & Johnson,L.R. (1976)
The tau method for inversion of travel times II. Earthquake data. Geophys. J. Roy. astron. Soc., V46, pp.87-108.

Braile,L.W. & Smith,R.B. (1975)
Guide to the interpretation of crustal refraction profiles. Geophys. J. Roy. astron. Soc., V40, pp.145-176.

Bullen,K.E. (1965)
An introduction to the theory of seismology. Cambridge University Press. 381pp.

Červený,V. & Ravindra,R. (1971)
Theory of seismic head waves. University of Toronto Press. 312pp.

Chapman,C.H. (1976a)
A first-motion alternative to geometrical ray theory. Geophys. Res. Lett., V3, pp.153-156.

----- (1976b)
Exact and approximate generalized ray theory in vertically inhomogeneous media. Geophys. J. Roy. astron. Soc., V46, pp.217-233.

Chase,R.L. (1977)
J. Tuzo Wilson knolls: Canadian hotspot. Nature, V266, pp.344-346.

----- Tiffin,D.L. & Murray,J.W. (1975)
The western Canadian continental margin, in Canada's Continental Margins and Offshore Petroleum Exploration, edited by C.J.Yorath, E.R.Parker, and D.J.Glass, Can. Soc. Petrol. Geol. Mem. 4, pp.701-721.

Christensen,N.I. & Salisbury,M.H. (1975)
Structure and constitution of the lower crust. Rev. Geophys. Sp. Phys., V13, pp.57-86.

Clowes,R.M. (1977)
A marine deep seismic sounding system. Can. J. Earth Sci., V14, pp.1276-1285.

Crosson,R.S. (1972)
Small earthquakes, structure and tectonics of the Puget-Sound region. Bull. Seism. Soc. Am., V62, pp.1133-1171.

Davis,E.E., Lister,C.R.B. & Lewis,B.T.R. (1976)
Seismic structure on Juan de Fuca ridge: ocean bottom seismometer results from the Median Valley. J. Geophys. Res., V81, pp.3541-3555.

Dickinson,W.R. (1976)
Sedimentary basins developed during evolution of Mesozoic-Cenozoic arc-trench system in western North America. Can. J. Earth Sci., V13, pp.1268-1287.

Flinn,E.A. (1965)
Signal analysis using rectilinearity and direction of particle motion. Proc. I.E.E.E., V53, pp.1874-1876.

Gerver,M. & Markushevich,V. (1966)
Determination of seismic wave velocity from the travel time curve. Geophys. J. Roy. astron. Soc.,V11, pp.165-173.

Griffin,J.N. (1966a)
Applications and development of polarization (REMODE) filters. Seismic data lab. report #141, Earth Science Division, Teledyne Inc.

----- (1966b)
Remode signal/noise tests in polarized noise. Seismic data lab. report #162, Earth Science Division, Teledyne Inc.

Heffler,D.E. & Locke,D.R. (1977)
A deep ocean release mechanism. Mar. Geophys. Res., V3, pp.229-232.

Houtz,R.E. (1976)
Seismic properties of layer 2A in the Pacific. J. Geophys. Res., V81, pp.6321-6340.

Hyndman,R.D., Rogers,G.C., Lister,C.R.B., Wade,U.S., Barrett,D.L., Davis,E.E., Lewis,T., Lynch,S. & Seeman,D. (1978)
Geophysical measurements in the region of the Explorer ridge off western Canada. Submitted to Can. J. Earth Sci.

Johnson,L.E. & Gilbert,F. (1972)
Inversion and inference for teleseismic ray data, in Methods in Computational Physics, V12, edited by B.A.Bolt, pp.231-266, Academic, New York.

Johnson II,R.V., Lister,C.R.B. & Lewis,B.T.R. (1977)
A direct recording ocean bottom seismometer. Mar. Geophys. Res., V3, pp.65-85.

Julian,B.R. & Anderson,D.L. (1968)
Travel times, apparent velocities and amplitudes of body waves. Bull. Seism. Soc. Am., V58, pp.339-366.

Kanasewich,E.R. (1975)
Time sequence analysis in geophysics (second edition). University of Alberta press. 364pp.

Keen,C.E. & Barrett,D.L. (1971)
A measurement of seismic anisotropy in the northeast Pacific. Can. J. Earth Sci., V8, pp.1056-1064.

----- & Tramontini,C. (1970)
A seismic refraction survey on the mid-Atlantic ridge. Geophys. J. Roy. astron. Soc., V20, pp.473-491.

Kennett,B.L.N. (1976)
A comparison of travel time inversions. Geophys. J. Roy. astron. Soc., V44, pp.517-536.

----- (1977)
Towards a more detailed seismic picture of the oceanic crust and mantle. Mar. Geophys. Res., V3, pp.7-42.

----- Bunch,A.W.H., Orcutt,J.A. & Raitt,R.W. (1977)
Variations in crustal structure on the East Pacific Rise crest: a travel time inversion approach. Earth Planet. Sci. Lett., V34, pp.439-444.

----- & Orcutt,J.A. (1976)
A comparison of travel time inversions for marine refraction profiles. J. Geophys. Res., V81, pp.4061-4040.

Le Pichon,X., Houtz,R.E., Drake,C.L. & Nafe,J.E. (1965)
Crustal structure of the mid-ocean ridges, 1, seismic refraction measurements. J. Geophys. Res., V70, pp.319-339.

Lewis,B.T.R. & McClain,J. (1977)
Converted shear waves as seen by ocean bottom seismometers and surface buoys. Bull. Seism. Soc. Am., V67, pp.1291-1302.

Lister,C.R.B. & Lewis,B.T.R. (1976)
An ocean-bottom seismometer suitable for arrays. Deep Sea Res., V23, pp.113-124.

Lynch,S. (1977)
The crustal structure of Winona Basin as determined by deep seismic sounding. Unpublished MSc thesis, University of British Columbia. 122pp.

Malecek,S.J. & Clowes,R.M. (1978)
Crustal structure near Explorer ridge from a marine deep seismic sounding survey. J. Geophys. Res. (in press)

McKenzie,D.P. & Morgan,W.J. (1969)
Evolution of triple junctions. Nature, V224, pp.125-133.

----- & Parker,R.L. (1967)
The North Pacific: an example of tectonics on a sphere. Nature, V216, pp.1276-1280.

McMechan,G.A. (1976)
Generalized p-Δ curves. Geophys. J. Roy. astron. Soc., V47, pp.9-18.

----- (1978)
Multiple water reflections recorded at the ocean bottom. Can. J. Earth Sci., V15, pp.78-85.

----- & Wiggins,R.A. (1972)
Depth limits in body wave inversion, Geophys. J. Roy. astron. Soc., V28, pp.459-473.

Montalbetti,J.F. & Kanasewich,E.R. (1970)
Enchancement of teleseismic body phases with a polarization filter. Geophys. J. Roy. astron. Soc., V21, pp.119-129.

O'Brien,P.N.S. (1967)
The efficient use of large charges, in Seismic Refraction Prospecting, edited by A.W.Musgrave. Society of Exploration Geophysicists. pp.152-170.

Orcutt,J.A., Kennett,B.L.N. & Dorman,L.M. (1976)
Structure of the East Pacific Rise from an ocean bottom seismometer survey. Geophys. J. Roy. astron. Soc., V45, pp.305-320.

Peterson,J.J., Fox,P.J. & Schreiber,E. (1974)
Newfoundland ophiolites and the geology of the oceanic layer. Nature, V247, pp.194-196.

Poehls,K. (1974)
Seismic refraction on the mid-Altantic ridge at 37°N. J. Geophys. Res., V79, pp.3370-3372.

Riddihough,R.P. (1977)
A model for recent plate interactions off Canada's west coast. Can. J. Earth Sci., V14, pp.384-396.

----- & Hyndman,R.D. (1976)
Canada's active western margin - the case for subduction. Geosci. Canada, V3, pp.269-278.

Salisbury,M.H. & Christensen,N.I. (1978)
The seismic velocity structure of a traverse through the Bay of Islands Ophiolite Complex, Newfoundland, an exposure of oceanic crust and upper mantle. J. Geophys. Res., V83, pp.805-817.

Sax,R.L. (1966)
Feasibility of linear polarization measurements for detecting and measuring seismic body waves. Seismic data lab. report #163, Earth Science Division, Teledyne Inc.

----- & Mims,C.H. (1965)
Rectilinear motion detection (REMODE), Seismic data lab. report #118, Earth Science Division, Teledyne Inc.

Shor,G.G.Jr. (1963)
Refraction and reflection techniques and procedure, in The Sea, edited by M.N.Hill. Interscience. pp.30-38.

Silver,E.A. (1971)
Small plate tectonics on the north-eastern Pacific. Bull. Geol. Soc. Amer., V82, pp.3491-3496.

Souriau,M. & Veinante,J.L. (1975)
Three adaptive filters for the detection of body waves with application to deep seismic soundings. Bull. Seism. Soc. Am., V65, pp.995-1012.

Spence,G.D. (1976)
Gravity and seismic studies in the Southern Rocky Mountain Trench. Unpublished MSc thesis, University of British Columbia. 84pp.

Srivastava,S.P. (1973)
Interpretation of gravity and magnetic measurements across the continental margin of British Columbia, Canada. Can. J. Earth Sci., V10, pp.1664-1677.

Stacey,R.A. (1973)
Gravity anomalies, crustal structure, and plate tectonics in the Canadian Cordillera. Can. J. Earth Sci., V10, pp.615-628.

Sutton,G.H., Kasahara,J., Ichinose,W.N. & Byrne,D.A. (1977)
Ocean bottom seismograph development at Hawaii Institute of Geophysics. Mar. Geophys. Res., V3, pp.153-177.

Talwani,M., Windisch,C.C. & Langseth,M.G. (1971)
Reykjanes ridge crest: a detailed geophysical study. J. Geophys. Res., V76, pp473-517.

Thorleifson,A.J. (1978)
A marine deep seismic sounding survey over Winona Basin. Unpublished MSc thesis, University of British Columbia, 70pp.

Tiffin,D.L. & Seemann,D. (1975)
Bathymetric map of the continental margin of western Canada, open file map, Geol. Surv. Canada.

Tobin,D.G. & Sykes,L.R. (1968)
Seismicity and the tectonics of the northern Pacific Ocean. J. Geophys. Res., V73, pp.3821-3845.

Vine,F.J. (1966)
Spreading of the ocean floor, new evidence. Science, V154, pp.1405-1415.

----- & Wilson,J.T. (1965)
Magnetic anomalies over a young oceanic ridge off Vancouver Island. Science, V150, pp.485-489.

----- & Matthews,D.H. (1963)
Magnetic anomalies over ocean ridges. Nature, V199, pp.947-949.

Whitmarsh, R.B. (1978)
Seismic refraction studies of the upper igneous crust in the North Atlantic and porosity estimates for layer 2. Earth Planet. Sci. Lett., V37, pp.451-464.

Wiggins,R.A. (1976)
Body wave amplitude calculations II. Geophys. J. Roy. astron. Soc., V46, pp.1-10.

----- & Madrid,J.A. (1974)
Body wave amplitude calculations. Geophys. J. Roy. astron. Soc., V37, pp.423-433.